Naval Research Laboratory
Washington, DC 20375-5320

NRL/5310/MR—2021/5

Finite-Difference Time-Domain Method with the Modified Assigned Material Parameters Concept

MICHAEL S. KLUSKENS

Radar Analysis Branch
Radar Division

May 25, 2021

REPORT DOCUMENTATION PAGE

Form Approved
OMB No. 0704-0188

1. REPORT DATE *(DD-MM-YYYY)*	**2. REPORT TYPE**	**3. DATES COVERED** *(From - To)*
25-05-2021	NRL Memorandum Report	Oct 2020 – May 2021

4. TITLE AND SUBTITLE

Finite-Difference Time-Domain Method with the Modified Assigned Material Parameters Concept

5a. CONTRACT NUMBER

5b. GRANT NUMBER

5c. PROGRAM ELEMENT NUMBER
PE-62271N

6. AUTHOR(S)

Michael S. Kluskens

5d. PROJECT NUMBER

5e. TASK NUMBER

5f. WORK UNIT NUMBER
6B47

7. PERFORMING ORGANIZATION NAME(S) AND ADDRESS(ES)

Naval Research Laboratory
4555 Overlook Avenue, SW
Washington, DC 20375-5320

8. PERFORMING ORGANIZATION REPORT NUMBER

NRL/5310/MR--2021/5

9. SPONSORING / MONITORING AGENCY NAME(S) AND ADDRESS(ES)

Office of Naval Research
One Liberty Center
875 N. Randolph Street, Suite 1425
Arlington, VA 22203-1995

10. SPONSOR / MONITOR'S ACRONYM(S)

ONR

11. SPONSOR / MONITOR'S REPORT NUMBER(S)

12. DISTRIBUTION / AVAILABILITY STATEMENT

DISTRIBUTION STATEMENT A: Approved for public release; distribution is unlimited.

13. SUPPLEMENTARY NOTES

14. ABSTRACT

This report presents the derivation and evaluation of the Modified Assigned Material Parameters (MAMP) concept as an extension of the finite-difference time-domain (FDTD) method for electromagnetic modeling. In the MAMP concept, a correction factor to the material parameters of a cell is calculated for structures in a cell, thereby accounting for nonlinear field distributions in the cell. As this is equivalent to a physical material, the resulting FDTD equations have the same stability constraints as Yee FDTD. To determine the MAMP coefficients around a cylinder, I use the characteristic near field of a metal cylinder which is derived in this report. To accurately evaluate the MAMP concept, I develop and evaluate enhancements to the total-field/scattered-field method for the generation of an incident plane-wave in two-dimensions. In addition, I show the errors from a conventional method for the evaluation of the scattered far-field versus alternatives. In summary, I show that MAMP concept provides some increase in accuracy for the scattering by small cylinders, but to be useful in general requires the quasistatic solution for general shapes and further improvement will require a different formulation of the MAMP concept.

15. SUBJECT TERMS

Finite-difference time-domain
Echo width
Total-field/Scattered-field
Modified assigned material parameters

16. SECURITY CLASSIFICATION OF:			**17. LIMITATION OF ABSTRACT**	**18. NUMBER OF PAGES**	**19a. NAME OF RESPONSIBLE PERSON**
					Michael S. Kluskens
a. REPORT	**b. ABSTRACT**	**c. THIS PAGE**	SAR	61	**19b. TELEPHONE NUMBER** *(include area code)*
U	U	U			(202) 404-1818

Standard Form 298 (Rev. 8-98)
Prescribed by ANSI Std. Z39.18

This page intentionally left blank.

CONTENTS

FIGURES

EXECUTIVE SUMMARY

This report presents the derivation and evaluation of the Modified Assigned Material Parameters (MAMP) concept as an extension of the finite-difference time-domain (FDTD) method for electromagnetic modeling. In the MAMP concept, a correction factor to the material parameters of a cell is calculated for structures in a cell, thereby accounting for nonlinear field distributions in the cell. As this is equivalent to a physical material, the resulting FDTD equations have the same stability constraints as Yee FDTD. To determine the MAMP coefficients around a cylinder, I use the characteristic near field of a metal cylinder which is derived in this report. To accurately evaluate the MAMP concept, I develop and evaluate enhancements to the total-field/scattered-field method for the generation of an incident plane-wave in two-dimensions. In addition, I show the errors from a conventional method for the evaluation of the scattered far-field versus alternatives. In summary, I show that MAMP concept provides some increase in accuracy for the scattering by small cylinders, but to be useful in general requires the quasistatic solution for general shapes and further improvement will require a different formulation of the MAMP concept.

This page intentionally left blank

FINITE-DIFFERENCE TIME-DOMAIN METHOD WITH THE MODIFIED ASSIGNED MATERIAL PARAMETERS CONCEPT

1. INTRODUCTION

This report is a continuation of report NRL/MR/5310–20-10,148 [1] with further derivation and evaluation of concepts in the finite-difference time-domain (FDTD) method.

1.1 Finite-Difference Time-Domain in Electromagnetics

All finite-difference time-domain derivations in electromagnetics originate from either the differential form of Maxwell's equations,

$$\nabla \times \boldsymbol{\mathcal{E}}(t) = -\frac{\partial \boldsymbol{\mathcal{B}}(t)}{\partial t}, \tag{1a}$$

$$\nabla \times \boldsymbol{\mathcal{H}}(t) = \frac{\partial \boldsymbol{\mathcal{D}}(t)}{\partial t} + \boldsymbol{\mathcal{J}}(t), \tag{1b}$$

$$\nabla \cdot \boldsymbol{\mathcal{D}}(t) = \rho(t), \tag{1c}$$

$$\nabla \cdot \boldsymbol{\mathcal{B}}(t) = 0, \tag{1d}$$

or the integral form of Maxwell's equations,

$$\oint \boldsymbol{\mathcal{E}}(t) \cdot d\mathbf{l} = -\frac{\partial}{\partial t} \iint \boldsymbol{\mathcal{B}}(t) \cdot d\mathbf{s}, \tag{2a}$$

$$\oint \boldsymbol{\mathcal{H}}(t) \cdot d\mathbf{l} = \frac{\partial}{\partial t} \iint \boldsymbol{\mathcal{D}}(t) \cdot d\mathbf{s} + \iint \boldsymbol{\mathcal{J}}(t) \cdot d\mathbf{s}, \tag{2b}$$

$$\oiint \boldsymbol{\mathcal{D}}(t) \cdot d\mathbf{s} = \iiint \rho(t)\, dv, \tag{2c}$$

$$\oiint \boldsymbol{\mathcal{B}}(t) \cdot d\mathbf{s} = 0, \tag{2d}$$

where $\boldsymbol{\mathcal{E}}/\boldsymbol{\mathcal{H}}$ are the electric/magnetic field intensities, $\boldsymbol{\mathcal{D}}/\boldsymbol{\mathcal{B}}$ are the electric/magnetic flux densities, and $\boldsymbol{\mathcal{J}}/\rho$ are the electric current/charge densities [2, Section 1-2], [3, Section 1.2]. As adding anisotropic materials to FDTD is a mathematical exercise and this report is focused on scattering from objects, the following derivations focus on isotropic materials without local current sources where I rearrange Equations (1a) – (1b) as follows

$$\mu \frac{\partial \boldsymbol{\mathcal{H}}(t)}{\partial t} + \sigma^* \boldsymbol{\mathcal{H}}(t) = -\nabla \times \boldsymbol{\mathcal{E}}(t), \tag{3a}$$

$$\epsilon \frac{\partial \boldsymbol{\mathcal{E}}(t)}{\partial t} + \sigma \boldsymbol{\mathcal{E}}(t) = \nabla \times \boldsymbol{\mathcal{H}}(t), \tag{3b}$$

Manuscript approved May 24, 2021.

where ϵ is the permittivity, μ is the permeability, σ is the effective electric conductivity, and σ^* is the effective magnetic conductivity. The effective conductivities contain a first-order approximation of the time-varying permittivity and permeability, respectively [1]. The remaining equations, Equations (1d) and (1c), are Gauss' Law for electric and magnetic charge and require free charge to be zero in a source-free region. By taking the divergence of Equations (1a) and (1b), it is seen that Equations (1d) and (1c) are redundant [4, Section 2.1].

1.2 Two-Dimensional Finite-Difference Time-Domain

The key concept in the 1966 paper by K. S. Yee proposing FDTD for electromagnetic modeling is the approximation of the partial derivatives in the differential form of Maxwell's equations by second order central differences, thereby yielding a method that is second-order accurate in space and time [5]. From Equation (3) the Yee FDTD update equations for a two-dimensional problem with the fields $\mathcal{E}_z(x, y, t)$, $\mathcal{H}_x(x, y, t)$, and $\mathcal{H}_y(x, y, t)$ in isotropic material are

$$\begin{aligned}\mathcal{E}_z(x,y,t) = c_a\mathcal{E}_z(x,y,t-\Delta t) \\ + \frac{c_b}{\Delta x}\left[\mathcal{H}_y(x+\tfrac{\Delta x}{2},y,t-\tfrac{\Delta t}{2}) - \mathcal{H}_y(x-\tfrac{\Delta x}{2},y,t-\tfrac{\Delta t}{2})\right] \\ - \frac{c_b}{\Delta y}\left[\mathcal{H}_x(x,y+\tfrac{\Delta y}{2},t-\tfrac{\Delta t}{2}) - \mathcal{H}_x(x,y-\tfrac{\Delta y}{2},t-\tfrac{\Delta t}{2})\right],\end{aligned} \tag{4a}$$

$$\mathcal{H}_x(x,y+\tfrac{\Delta y}{2},t+\tfrac{\Delta t}{2}) = d_{ax}\mathcal{H}_x(x,y+\tfrac{\Delta y}{2},t-\tfrac{\Delta t}{2}) - \frac{d_{bx}}{\Delta y}\left[\mathcal{E}_z(x,y+\Delta y,t) - \mathcal{E}_z(x,y,t)\right], \tag{4b}$$

$$\mathcal{H}_y(x+\tfrac{\Delta x}{2},y,t+\tfrac{\Delta t}{2}) = d_{ay}\mathcal{H}_y(x+\tfrac{\Delta x}{2},y,t-\tfrac{\Delta t}{2}) + \frac{d_{by}}{\Delta x}\left[\mathcal{E}_z(x+\Delta x,y,t) - \mathcal{E}_z(x,y,t)\right], \tag{4c}$$

where Δt is the time step, $(\Delta x, \Delta y)$ are the spatial step in the (x, y) directions, and (c_a, c_b, d_a, d_b) are the Yee FDTD equation parameters given by

$$c_a = \frac{2\epsilon - \sigma\Delta t}{2\epsilon + \sigma\Delta t}, \tag{5a}$$

$$c_b = \frac{2\Delta t}{2\epsilon + \sigma\Delta t}, \tag{5b}$$

$$d_a = \frac{2\mu - \sigma^*\Delta t}{2\mu + \sigma^*\Delta t}, \tag{5c}$$

$$d_b = \frac{2\Delta t}{2\mu + \sigma^*\Delta t}, \tag{5d}$$

with the material parameters defined at (x, y) for (c_a, c_b), at $(x, y+\frac{\Delta y}{2})$ for (d_{ax}, d_{bx}), and at $(x+\frac{\Delta x}{2}, y)$ for (d_{ay}, d_{by}). Some advanced FDTD techniques require the modification of the FDTD parameters; however, for stability I need to calculate the propagation velocity from the material parameters. In that case, the

material parameters can be calculated from the Yee FDTD equation parameters by

$$\epsilon = \Delta t \frac{1 + c_a}{2c_b}, \tag{6a}$$

$$\mu = \Delta t \frac{1 + d_a}{2d_b}, \tag{6b}$$

$$\sigma = \frac{1 - c_a}{c_b}, \tag{6c}$$

$$\sigma^* = \frac{1 - d_a}{d_b}. \tag{6d}$$

The Yee FDTD update equations for a two-dimensional problem with the fields H_z, E_x, and E_y are derived either directly from Equation (3) or from Equation (4) using duality [2, Section 3-2], [3, Section 7.2]. In addition, it has been shown that the Yee FDTD equations directly satisfy Equations (1d) and (1c) [6, Section 3.6.9]. A key parameter in FDTD is the time step, Δt. For two-dimensional Yee FDTD, the maximum time step for numerical stability in free space is [6, Section 4.7]

$$\Delta t = \frac{\Delta x \Delta y}{c\sqrt{\Delta x^2 + \Delta y^2}}, \tag{7}$$

where c is the speed of light.

These derivations are based on the differential form of Maxwell's equations, which are only valid where the fields are continuous and have continuous derivatives; however, neither are true at material interfaces [2, Section 1-2], [3, Section 1.2.1]. The reason Yee FDTD is not affected by these limitations is that the same equations are derived from the integral form of Maxwell's equations [6, Section 3.6.8]. If I linearly approximate the fields and evaluate Equation (2b) over a Δx by Δy square centered at (x, y), then taking $\mathcal{E}_z$ to be the value of the linear approximation at (x, y), and taking $\mathcal{H}_x$ and $\mathcal{H}_y$ to be the value of the linear approximations at the center of their respective edges, I derive Equation (4a) and conclude that it is second order accurate. Conversely, if I approximated the fields as constants over the square, I would incorrectly conclude that Equation (4a) was only first-order accurate.

2. TOTAL-FIELD/SCATTERED-FIELD METHOD IN TWO DIMENSIONS

The total-field/scattered-field (TF/SF) method is a technique to simulate scattering calculations in FDTD by dividing the FDTD space into total-field and scattered-field regions [6, Section 5.6], [7–16]. The scattered-field region surrounds the total-field region and the incident-field enters into the FDTD equations at the boundary between the two regions. I presented a detailed explanation and derivation for the one-dimensional TF/SF problem in [1]. From Equation (4) and following the approach in [1, Sec. 2], where the $\mathcal{E}_z$ fields are at the edge of the total-field region, the field corrections for the left boundary (x_m), right boundary (x_p), bottom boundary (y_m), and top boundary (y_p) are

$$\mathcal{E}_z^t(x_m, y, t) = \mathcal{E}_z^{t'}(x_m, y, t) - \frac{c_b}{\Delta x}\mathcal{H}_y^i(x_m - \tfrac{\Delta x}{2}, y, t - \tfrac{\Delta t}{2}), \tag{8a}$$

$$\mathcal{E}_z^t(x_p, y, t) = \mathcal{E}_z^{t'}(x_p, y, t) + \frac{c_b}{\Delta x}\mathcal{H}_y^i(x_p + \tfrac{\Delta x}{2}, y, t - \tfrac{\Delta t}{2}), \tag{8b}$$

$$\mathcal{E}_z^t(x, y_m, t) = \mathcal{E}_z^{t'}(x, y_m, t) + \frac{c_b}{\Delta x}\mathcal{H}_x^i(x, y_m - \tfrac{\Delta y}{2}, t - \tfrac{\Delta t}{2}), \tag{8c}$$

$$\mathcal{E}_z^t(x, y_p, t) = \mathcal{E}_z^{t'}(x, y_p, t) - \frac{c_b}{\Delta x}\mathcal{H}_x^i(x, y_p + \tfrac{\Delta y}{2}, t - \tfrac{\Delta t}{2}), \tag{8d}$$

$$\mathcal{H}_y^s(x_m - \tfrac{\Delta x}{2}, y, t + \tfrac{\Delta t}{2}) = \mathcal{H}_y^{s'}(x_m - \tfrac{\Delta x}{2}, y, t + \tfrac{\Delta t}{2}) - \frac{d_{by}}{\Delta x}\mathcal{E}_z^i(x_m, y, t), \tag{8e}$$

$$\mathcal{H}_y^s(x_p + \tfrac{\Delta x}{2}, y, t + \tfrac{\Delta t}{2}) = \mathcal{H}_y^{s'}(x_p + \tfrac{\Delta x}{2}, y, t + \tfrac{\Delta t}{2}) + \frac{d_{by}}{\Delta x}\mathcal{E}_z^i(x_p, y, t), \tag{8f}$$

$$\mathcal{H}_x^s(x, y_m - \tfrac{\Delta y}{2}, t + \tfrac{\Delta t}{2}) = \mathcal{H}_x^{s'}(x, y_m - \tfrac{\Delta y}{2}, t + \tfrac{\Delta t}{2}) + \frac{d_{bx}}{\Delta x}\mathcal{E}_z^i(x, y_m, t), \tag{8g}$$

$$\mathcal{H}_x^s(x, y_p + \tfrac{\Delta y}{2}, t + \tfrac{\Delta t}{2}) = \mathcal{H}_x^{s'}(x, y_p + \tfrac{\Delta y}{2}, t + \tfrac{\Delta t}{2}) - \frac{d_{bx}}{\Delta x}\mathcal{E}_z^i(x, y_p, t), \tag{8h}$$

where $\mathcal{E}_z^t$ is the electric field in the total-field region, $\mathcal{H}_x^s$ and $\mathcal{H}_y^s$ are the magnetic fields in the scattered-field region, and $\mathcal{E}_z^{t'}$, $\mathcal{H}_x^{s'}$ and $\mathcal{H}_y^{s'}$ represent the corresponding uncorrected fields. To minimize noise, the first non-zero field correction should occur with the $\mathcal{E}_z^t$ correction and not the $\mathcal{H}^s$ corrections, as the latter would generate an artificial field in the scattered-field region. The incident fields, $\mathcal{E}_z^i$, $\mathcal{H}_x^i$, $\mathcal{H}_y^i$, could be generated analytically; however, dispersion in the Yee FDTD grid creates noise at the TF/SF boundary as the fields travel at frequency dependent velocities in the FDTD grid [1, Sec. 2.2], [7, 8]. Instead, I use a one-dimensional Yee FDTD grid to generate the incident fields, and through a modification of the Yee FDTD update equations, I align the one-dimensional dispersion with the dispersion of the two-dimensional FDTD grid. To minimize noise in the one-dimensional Yee FDTD grid, I terminate each end with the cosine tapered perfectly matched layer (PML) detailed in [1, Sec. 6.3] and add a modulated Gaussian pulse at the edge of the $-x$ PML region. I modified the one-dimensional Yee FDTD update equations as follows

$$\mathcal{E}_z^{1D}(x, t+\Delta t) = c_a\mathcal{E}_z^{1D}(x, t) + f(\phi^i)\frac{c_b}{\Delta x}\left[\mathcal{H}_y^{1D}(x+\tfrac{\Delta x}{2}, t+\tfrac{\Delta t}{2}) - \mathcal{H}_y^{1D}(x-\tfrac{\Delta x}{2}, t+\tfrac{\Delta t}{2})\right], \tag{9a}$$

$$\mathcal{H}_y^{1D}(x+\tfrac{\Delta x}{2}, t+\tfrac{\Delta t}{2}) = d_a\mathcal{H}_y^{1D}(x+\tfrac{\Delta x}{2}, t-\tfrac{\Delta t}{2}) + f(\phi^i)\frac{d_b}{\Delta x}\left[\mathcal{E}_z^{1D}(x+\Delta x, t) - \mathcal{E}_z^{1D}(x, t)\right], \tag{9b}$$

where $f(\phi^i)$ is a dispersion correction factor dependent on the incidence angle ϕ^i. As the pulse propagating in the $-x$ direction is absorbed by the $-x$ PML region, I only have a pulse propagating in the $+x$ direction in the one-dimensional Yee FDTD grid. With ϕ^i as the incidence angle for the two-dimensional Yee FDTD grid, the pulse propagates in the $-x$ direction for $\phi^i = 0$. Therefore, after accounting for the propagation direction in the one-dimensional Yee FDTD grid and the definition of the incidence angle ϕ^i, I have

$$\mathcal{E}_z^i(x, y, t) = \mathcal{E}_z^{1D}(s, t), \tag{10a}$$

$$\mathcal{H}_x^i(x, y, t) = \mathcal{H}_y^{1D}(s, t)\sin\phi^i, \tag{10b}$$

$$\mathcal{H}_y^i(x, y, t) = -\mathcal{H}_y^{1D}(s, t)\cos\phi^i, \tag{10c}$$

where s is the location in the one-dimensional Yee FDTD grid that corresponds to a (x, y) point in the two-dimensional Yee FDTD grid and is given by

$$s(x, y) = (x_o - x)\cos\phi^i + (y_o - y)\sin\phi^i + s_o, \tag{11}$$

where (x_o, y_o) are offsets dependent on the incidence angle ϕ^i, and s_o is the offset to account for the PML layer at the end of the one-dimensional Yee FDTD grid. The offsets are determined as follows

$$x_o = \begin{cases} x_p & \text{if } \cos\phi^i \geq 0, \\ x_m & \text{otherwise,} \end{cases} \tag{12a}$$

$$y_o = \begin{cases} y_p & \text{if } \sin\phi^i \geq 0, \\ y_m & \text{otherwise,} \end{cases} \tag{12b}$$

and s_o is four plus the number of cells in the PML layer of the one-dimensional Yee FDTD grid. Then I write Equations (8a) – (8h) as

$$\mathcal{E}_z^t(x_m, y, t+\Delta t) = \mathcal{E}_z^{t'}(x_m, y, t+\Delta t) + \frac{c_b}{\Delta x}\mathcal{H}_y^{1D}\left[s(x_m - \tfrac{\Delta x}{2}, y), t+\tfrac{\Delta t}{2}\right]\cos\phi^i, \tag{13a}$$

$$\mathcal{E}_z^t(x_p, y, t+\Delta t) = \mathcal{E}_z^{t'}(x_p, y, t+\Delta t) - \frac{c_b}{\Delta x}\mathcal{H}_y^{1D}\left[s(x_p + \tfrac{\Delta x}{2}, y), t+\tfrac{\Delta t}{2}\right]\cos\phi^i, \tag{13b}$$

$$\mathcal{E}_z^t(x, y_m, t+\Delta t) = \mathcal{E}_z^{t'}(x, y_m, t+\Delta t) + \frac{c_b}{\Delta x}\mathcal{H}_y^{1D}\left[s(x, y_m - \tfrac{\Delta y}{2}), t+\tfrac{\Delta t}{2}\right]\sin\phi^i, \tag{13c}$$

$$\mathcal{E}_z^t(x, y_p, t+\Delta t) = \mathcal{E}_z^{t'}(x, y_p, t+\Delta t) - \frac{c_b}{\Delta x}\mathcal{H}_y^{1D}\left[s(x, y_p + \tfrac{\Delta y}{2}), t+\tfrac{\Delta t}{2}\right]\sin\phi^i, \tag{13d}$$

$$\mathcal{H}_y^s(x_m - \tfrac{\Delta x}{2}, y, t+\tfrac{\Delta t}{2}) = \mathcal{H}_y^{s'}(x_m - \tfrac{\Delta x}{2}, y, t+\tfrac{\Delta t}{2}) - \frac{d_{by}}{\Delta x}\mathcal{E}_z^{1D}\left[s(x_m, y), t\right], \tag{13e}$$

$$\mathcal{H}_y^s(x_p + \tfrac{\Delta x}{2}, y, t+\tfrac{\Delta t}{2}) = \mathcal{H}_y^{s'}(x_p + \tfrac{\Delta x}{2}, y, t+\tfrac{\Delta t}{2}) + \frac{d_{by}}{\Delta x}\mathcal{E}_z^{1D}\left[s(x_p, y), t\right], \tag{13f}$$

$$\mathcal{H}_x^s(x, y_m - \tfrac{\Delta y}{2}, t+\tfrac{\Delta t}{2}) = \mathcal{H}_x^{s'}(x, y_m - \tfrac{\Delta y}{2}, t+\tfrac{\Delta t}{2}) + \frac{d_{bx}}{\Delta x}\mathcal{E}_z^{1D}\left[s(x, y_m), t\right], \tag{13g}$$

$$\mathcal{H}_x^s(x, y_p + \tfrac{\Delta y}{2}, t+\tfrac{\Delta t}{2}) = \mathcal{H}_x^{s'}(x, y_p + \tfrac{\Delta y}{2}, t+\tfrac{\Delta t}{2}) - \frac{d_{bx}}{\Delta x}\mathcal{E}_z^{1D}\left[s(x, y_p), t\right]. \tag{13h}$$

For $\phi^i = 0°, 90°, 180°$, and $270°$ the dispersion in the two-dimensional Yee FDTD grid is identical to that in the one-dimensional grid with the same Δx so no correction is needed when $\Delta x = \Delta y$. For a first example, I present results in Figure 1 for $\phi^i = 0°$ and $f(\phi^i) = 1$ after 10 and 30 nanoseconds (ns) where the value of the incident fields $(\mathcal{E}_z^i, \mathcal{H}_x^i, \mathcal{H}_y^i)$ is taken from the nearest field point $(\mathcal{E}_z^{1D}, \mathcal{H}_y^{1D})$ in the one-dimensional Yee FDTD grid. At a graphical level I see no leakage from the total-field region into the scattered-field region. In Figure 2, I compare the results generated using the nearest field point versus cubic interpolation of the one-dimensional Yee FDTD grid at 40 ns, which is after the Gaussian pulse has passed the $-x$ boundary at the edge of the total-field region. In both cases I see residual field errors on the order of 0.007% of the magnitude of the Gaussian pulse. In order to numerically evaluate the errors for off-axis propagation I detail the calculation of scattered-fields in the next section.

a) TF/SF Plane Wave From Nearest One-Dimensional FDTD Grid Point, Time=10 ns

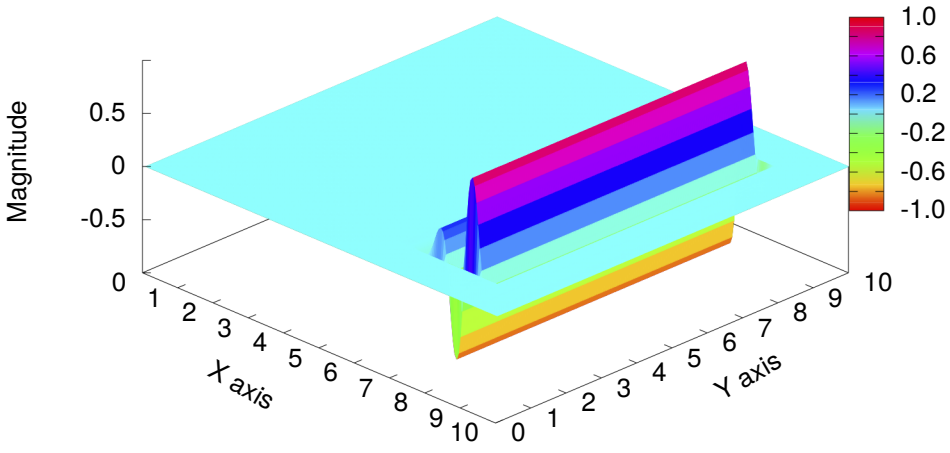

b) TF/SF Plane Wave From Nearest One-Dimensional FDTD Grid Point, Time=30 ns

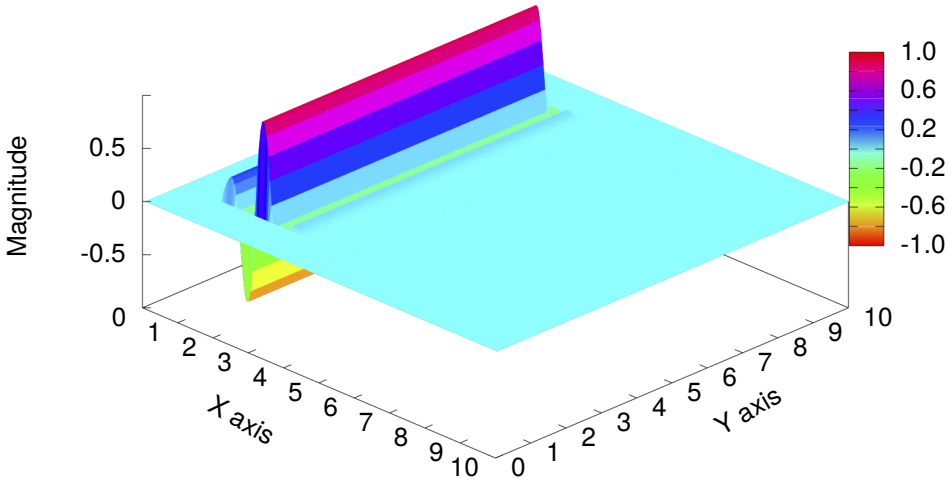

Fig. 1—Total-field/scattered-field generation of a modulated Gaussian plane wave (f_c = 300 MHz, f_{BW} = 300 MHz) in a two-dimensional Yee FDTD grid, for $\phi^i = 0°$, after (a) 10 ns and (b) 30 ns with Δx = 0.05 meters and $\Delta t = \Delta x/(c\sqrt{2})$.

a) TF/SF Plane Wave From Nearest One-Dimensional FDTD Grid Point, Time=40 ns

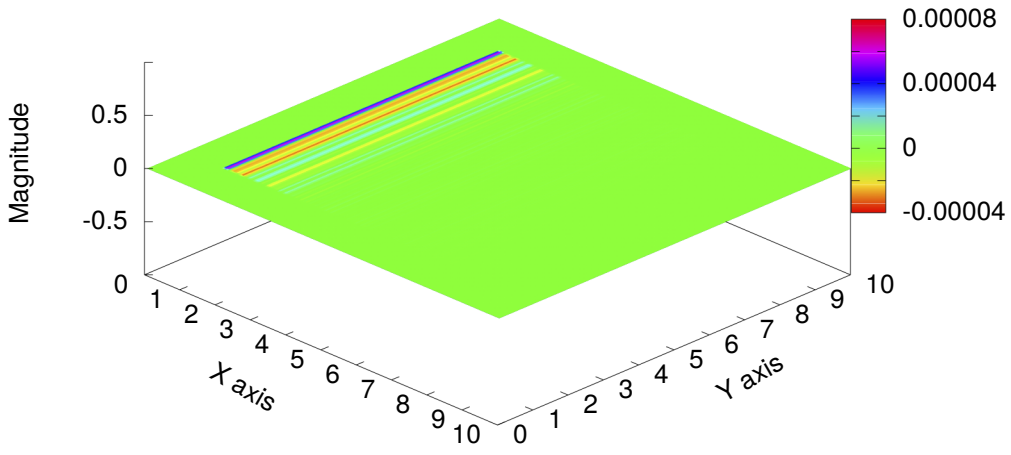

b) TF/SF Plane Wave With Cubic Interpolation of One-Dimensional FDTD Grid, Time=40 ns

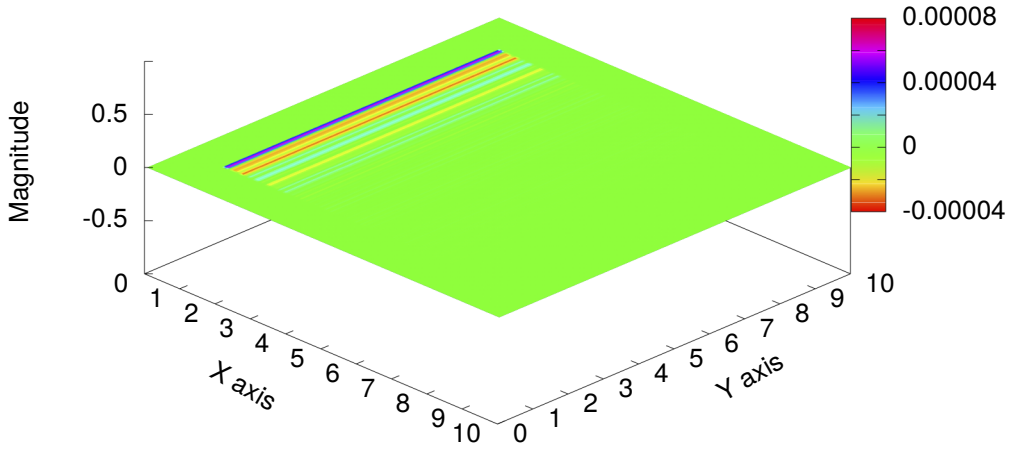

Fig. 2—Total-field/scattered-field generation of a modulated Gaussian plane wave (f_c = 300 MHz, f_{BW} = 300 MHz) in a two-dimensional Yee FDTD grid, for $\phi^i = 0°$, after 40 ns for (a) no interpolation versus (b) cubic interpolation for $\Delta x = 0.05$ meters and $\Delta t = \Delta x/(c\sqrt{2})$.

3. CALCULATION OF SCATTERED FIELDS

In this section I detail the calculation of fields scattered by an object in a Yee FDTD grid, also known as a near to far-field transformation [6, Chapter 8]. From the surface equivalence theorem, outlined in Figure 3 [2, Section 3-5], [3, Section 7.8], I know that the fields $(\mathbf{E}, \mathbf{H})$ due to currents inside a region, $\mathcal{R}$, can be determined from equivalent currents $(\mathbf{J}, \mathbf{M})$ on surface $\mathcal{S}$ of the region.

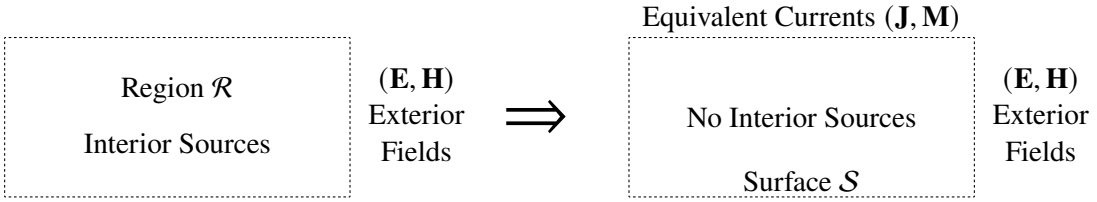

Fig. 3—Summary of surface equivalence theorem

The equivalent currents $(\mathbf{J}, \mathbf{M})$ are given by [3, Equation 7-43]

$$\mathbf{J} = \hat{n} \times \mathbf{H}, \tag{14a}$$

$$\mathbf{M} = -\hat{n} \times \mathbf{E}, \tag{14b}$$

where $\hat{n}$ is the outward normal to the surface and $(\mathbf{E}, \mathbf{H})$ are the fields on the surface. From these currents I could directly calculate the scattered fields in free space using two-dimensional far-field radiation equations [3, Section 11.2.1]; however, this approach limits me to the calculation of the far-field scattered fields in free space only. With application of image theory [2, Section 3-4], [3, Section 7.4] I could calculate the scattered fields in the presence of a perfectly conducting ground plane; however, the presence of a lossy multilayer media such as in geophysics applications [9, 11, 17–21] is substantially more complicated with this approach.

As an alternative, from the reciprocity theorem [2, Section 3-8], [3, Section 7.5] I know that I can determine the electric field $\mathbf{E}_P$ at point P in Figure 4a due to the equivalent currents $(\mathbf{J}, \mathbf{M})$ on surface $\mathcal{S}$ using the reciprocal problem shown in Figure 4b. In the reciprocal problem I determine the fields $(\mathbf{E}^R, \mathbf{H}^R)$

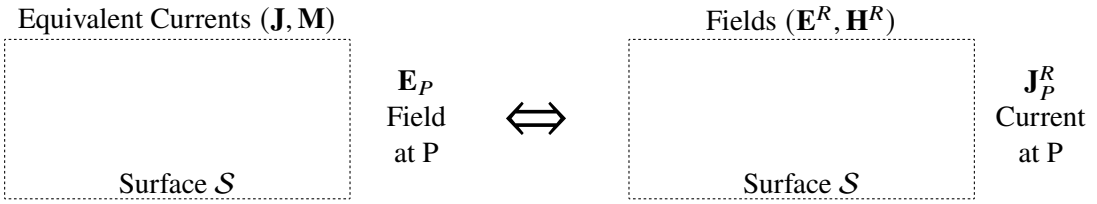

(a) Equivalent Problem (b) Reciprocal Problem

Fig. 4—Two problems of identical geometry connected by the reciprocity theorem

incident on surface $\mathcal{S}$ due to the electric current $\mathbf{J}_P^R$ at point P. The reciprocity theorem defines the relation

between two problems of identical geometry but with different currents and fields. From [3, Equation 7-32a], I write a special case of the reciprocity theorem with an electric current line source and zero magnetic currents in the reciprocal problem as

$$\mathbf{E}_P \cdot \mathbf{J}_P^R = \oiint_S \left[\mathbf{E}^R \cdot \mathbf{J} - \mathbf{H}^R \cdot \mathbf{M}\right] ds. \tag{15}$$

For this two-dimensional problem I only have the z-component of the electric field; therefore, I take $\mathbf{J}_P^R$ to be a unit-amplitude z-directed line source. Then, I reduce the reciprocity theorem to

$$E_z = \oiint_S \left[\mathbf{E}^R \cdot (\hat{n} \times \mathbf{H}) + \mathbf{H}^R \cdot (\hat{n} \times \mathbf{E})\right] ds. \tag{16}$$

Now I need the fields $(\mathbf{E}^R, \mathbf{H}^R)$ from the unit amplitude z-directed electric line source, which in the far-field are given by [3, Equation 11-13]

$$\mathbf{E}^R = \hat{z}\eta_0 \sqrt{\frac{k_0}{8\pi}} \frac{e^{-jk_0\rho}}{\sqrt{\rho}}, \tag{17a}$$

$$\mathbf{H}^R = -\hat{\phi} \sqrt{\frac{k_0}{8\pi}} \frac{e^{-jk_0\rho}}{\sqrt{\rho}}, \tag{17b}$$

where $\eta_0 = \sqrt{\mu_0/\epsilon_0}$ is the wave impedance of free space, $k_0 = 2\pi/\lambda_0$ is the wavenumber in free space, λ_0 is wavelength in freespace, and ρ is the distance in the standard cylindrical coordinate system defined by (ϕ,ρ). Next, I convert Equation (17) to rectangular coordinates and take the line source to the far-field so that I get the plane wave defined by

$$\mathbf{E}^R = \hat{z}\eta_0 E^R(x, y), \tag{18a}$$

$$\mathbf{H}^R = \Big(-\hat{x}\sin(\phi^s) + \hat{y}\cos(\phi^s)\Big) E^R(x, y), \tag{18b}$$

where ϕ^s is the scattered field angle and $E^R(x, y)$ is the scalar component of the reciprocal incident electric field at (x, y), given by

$$E^R(x, y) = \sqrt{\frac{k_0}{8\pi}} e^{jk_0[x\cos(\phi^s) + y\sin(\phi^s)]}. \tag{19}$$

Then I can write the far-field for the equivalent currents on a two-dimensional box as

$$E_z^P = \int_{y_m}^{y_p} E^R(x_m, y) \left[\hat{z} \cdot \Big(-\hat{x} \times \hat{y}\, H_y(x_m, y)\Big) + \hat{y}\frac{\cos(\phi^s)}{\eta_0} \cdot \Big(-\hat{x} \times \hat{z}\, E_z(x_m, y)\Big)\right] dy \tag{20a}$$

$$+ \int_{y_m}^{y_p} E^R(x_p, y) \left[\hat{z} \cdot \Big(\hat{x} \times \hat{y}\, H_y(x_p, y)\Big) + \hat{y}\frac{\cos(\phi^s)}{\eta_0} \cdot \Big(\hat{x} \times \hat{z}\, E_z(x_p, y)\Big)\right] dy \tag{20b}$$

$$+ \int_{x_m}^{x_p} E^R(x, y_m) \left[\hat{z} \cdot \Big(-\hat{y} \times \hat{x}\, H_x(x, y_m)\Big) - \hat{x}\frac{\sin(\phi^s)}{\eta_0} \cdot \Big(-\hat{y} \times \hat{z}\, E_z(x, y_m)\Big)\right] dx \tag{20c}$$

$$+ \int_{x_m}^{x_p} E^R(x, y_p) \left[\hat{z} \cdot \Big(\hat{y} \times \hat{x}\, H_x(x, y_p)\Big) - \hat{x}\frac{\sin(\phi^s)}{\eta_0} \cdot \Big(\hat{y} \times \hat{z}\, E_z(x, y_p)\Big)\right] dx, \tag{20d}$$

where all terms that would evaluate to zero have been removed. Then I can reduce Equation (20) to

$$E_z^P = \int_{y_m}^{y_p} E^R(x_m, y) \left[-H_y(x_m, y) + \frac{\cos(\phi^s)}{\eta_0} E_z(x_m, y) \right] dy \tag{21a}$$

$$+ \int_{y_m}^{y_p} E^R(x_p, y) \left[H_y(x_p, y) - \frac{\cos(\phi^s)}{\eta_0} E_z(x_p, y) \right] dy \tag{21b}$$

$$+ \int_{x_m}^{x_p} E^R(x, y_m) \left[H_x(x, y_m) + \frac{\sin(\phi^s)}{\eta_0} E_z(x, y_m) \right] dx \tag{21c}$$

$$+ \int_{x_m}^{x_p} E^R(x, y_p) \left[-H_x(x, y_p) - \frac{\sin(\phi^s)}{\eta_0} E_z(x, y_p) \right] dx, \tag{21d}$$

where E_z, H_x, and H_y are frequency-domain fields obtained from the Fourier transform of $\mathcal{E}_z$, $\mathcal{H}_x$, and $\mathcal{H}_y$ from the two-dimensional Yee FDTD grid.

I can align the integration surface $\mathcal{S}$ with either the E_z electric or the (H_x, H_y) magnetic grid points. As a starting point, I align the integration surface with the magnetic fields and linearly interpolate the electric fields while using a mid-point Riemann sum for the integration [22, Equation 1.2.3]. In Section 8.1, I align the integration surface with the E_z fields and compare the accuracy between these two approaches.

In two-dimensional scattering problems results are plotted in terms of echo width, σ_{2D} [2, Section 7-10], [3, Section 11.3]. Relative to E_z and E^i in this report, echo width is defined as

$$\sigma_{2D} = \lim_{\rho \to \infty} 2\pi\rho \left| \frac{E_z}{E^i} \right|^2. \tag{22}$$

As an example of a scattered field calculation, Figure 5 shows the echo width of a 1 meter by 1 meter square metal cylinder at 300 MHz. The calculation was performed with a Gaussian pulse with a center frequency of 300 MHz and a bandwidth of 300 MHz, so the echo width could be calculated for any frequency between 150 MHz and 450 MHz. The Yee FDTD grid at 25 ns is shown in Figure 6. The FDTD cell size is 0.05 meters with a 16 cell thick cosine PML region around the entire two-dimensional Yee FDTD grid, which is 200 cells square. The integration surface is 4 cells in from the surface of the PML region with the TF/SF boundary 3 cells in from the integration surface. The spacing between the integration surface and the TF/SF boundary has to be far enough to avoid the interpolation for the integration surface crossing into the total-field region.

4. BACKGROUND NOISE FROM TOTAL-FIELD/SCATTERED-FIELD BOUNDARY

The scattered field calculation is based on fields that pass through the TF/SF boundary into the scattered field region. Ideally these would only be fields scattered from objects in the total-field region; however, any imperfection in the TF/SF boundary will result in noise in the scattered field calculation and in this section I use that to evaluate the quality of the TF/SF boundary. I show in Figure 7 a noise floor of -120 dB for the same FDTD geometry and parameters as in Figures 5 – 6. The noise floor is determined by calculating the scattered field with the same parameters as in Figures 5 – 6, but without the metal cylinder. Two factors make this the best test case for determining if the TF/SF boundary is precisely implemented [7, 8]. The first factor is that the dispersion correction factor, $f(\phi^i)$, equals 1 as the dispersion in the two-dimensional

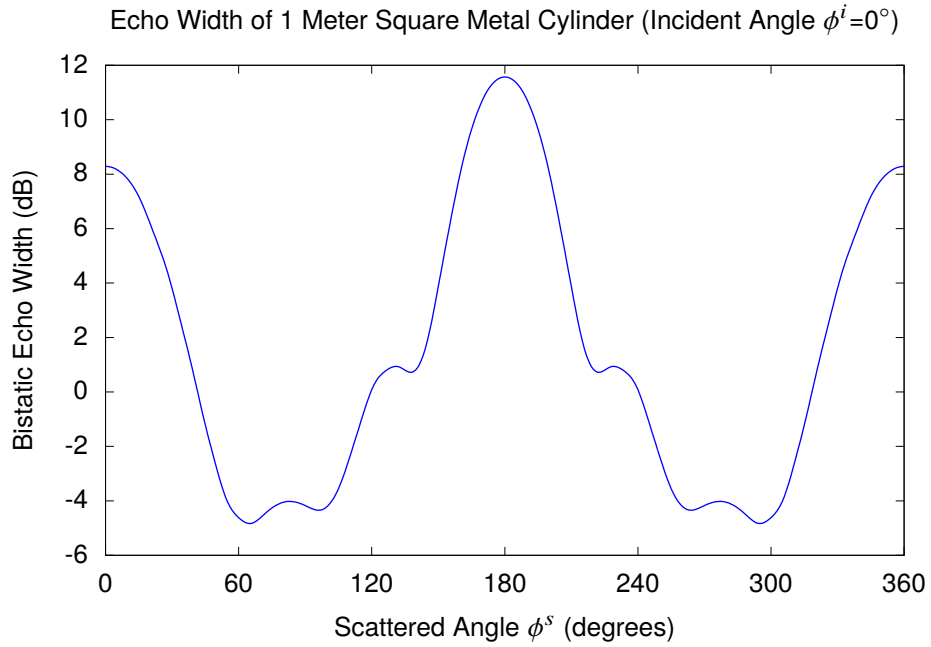

Fig. 5—Bistatic echo width of a 1 meter metal square cylinder at 300 MHz for a Yee FDTD grid with $\Delta x = 0.05$ meters, 800 time steps, a 16-cell cosine PML, 4 cells between the PML and integration surface, and 3 cells between the integration surface and the TF/SF boundary.

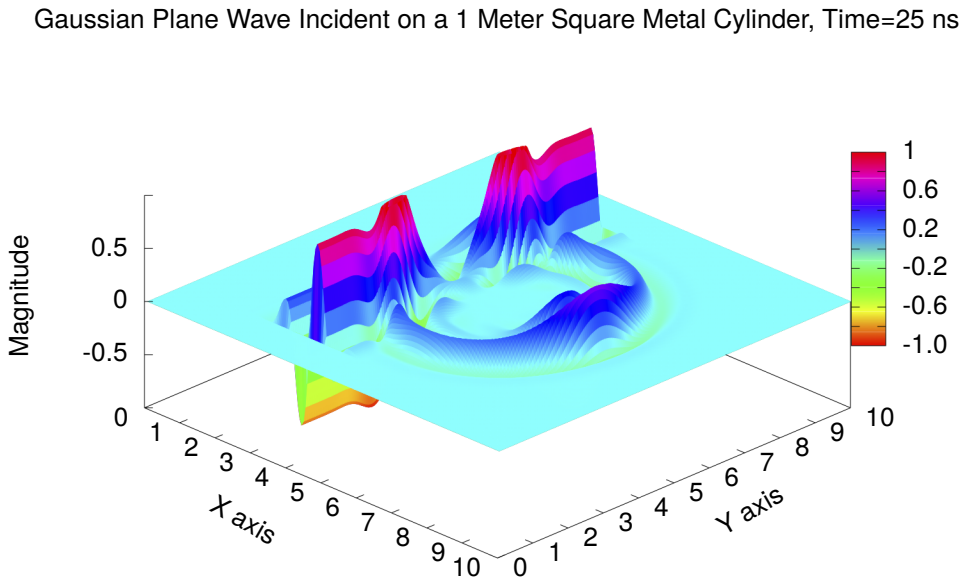

Fig. 6—Gaussian plane wave incident from $\phi^i = 0$ on a 1 meter metal square cylinder in a Yee FDTD grid with $\Delta x = 0.05$ meters and a 16-cell cosine PML.

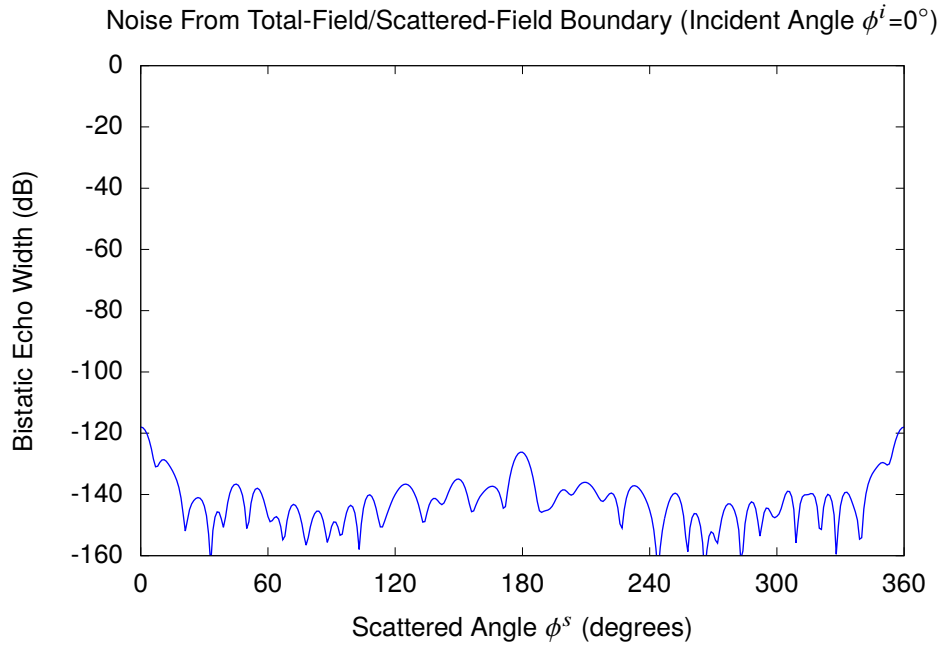

Fig. 7—Bistatic noise at 300 MHz for a Yee FDTD grid with $\Delta x = 0.05$ meters, 800 time steps, a 16-cell cosine PML, 4 cells between the PML and integration surface, and 3 cells between the integration surface and the TF/SF boundary.

Yee FDTD grid for $\phi^i = 0$ is identical at all frequencies to that in the one-dimensional Yee FDTD grid which is the source of the plane wave at the TF/SF boundary. Even numerical round-off error resulting in $f(\phi^i) = 1.000001$ raises the noise floor from -120 dB to -60 dB in this example. The second factor is that with careful alignment of the one-dimensional Yee FDTD grid with the TF/SF boundary points, all the $\mathcal{E}_z$ and $\mathcal{H}_y$ field points on the boundary align exactly with points in the one-dimensional Yee FDTD grid. This leaves only the $\mathcal{H}_x$ field points to be interpolated. In this first test case, as in Figures 5 – 6, I used the point nearest to the desired field point. Because of the limited number of points to be interpolated changing to a cubic interpolation had no effect on the calculations within 7 significant digits. However, changing ϕ^i to 45° changes $f(\phi^i)$ to 1.002081 for $\Delta x = 0.05$ meters and only for a frequency of 300 MHz. As a result, the difference in dispersion between the one-dimensional Yee FDTD grid and the two-dimensional Yee FDTD grid is not fully accounted for. In addition, as shown in Figure 8, the type of interpolation makes a large difference for off-axis propagation as all field points are interpolated. Using the nearest point from the one-dimensional Yee FDTD grid has the worse noise floor at around -20 dB. Linear and parabolic interpolation have very similar noise floors around -60 dB except near the forward direction of $\phi^s = 225°$ where they peak at -35 dB. Similarly, cubic interpolation and an average parabolic interpolation both have a noise floor of approximately -90 to -80 dB depending on angle with an increased noise floor around the forward direction also peaking at -35 dB. Both the cubic interpolation and the average parabolic interpolation use four points centered around the target point. Cubic interpolation is a single cubic polynomial fitting the four points. The average parabolic interpolation is the average of two independent parabolic interpolations, one using the first three points and the second using the last three of the four points. My purpose in this comparison is that higher order polynomial interpolation can introduce artificial swings in the data which an averaged parabolic interpolation should be less prone to; however, this test shows that the cubic interpolation is slightly better.

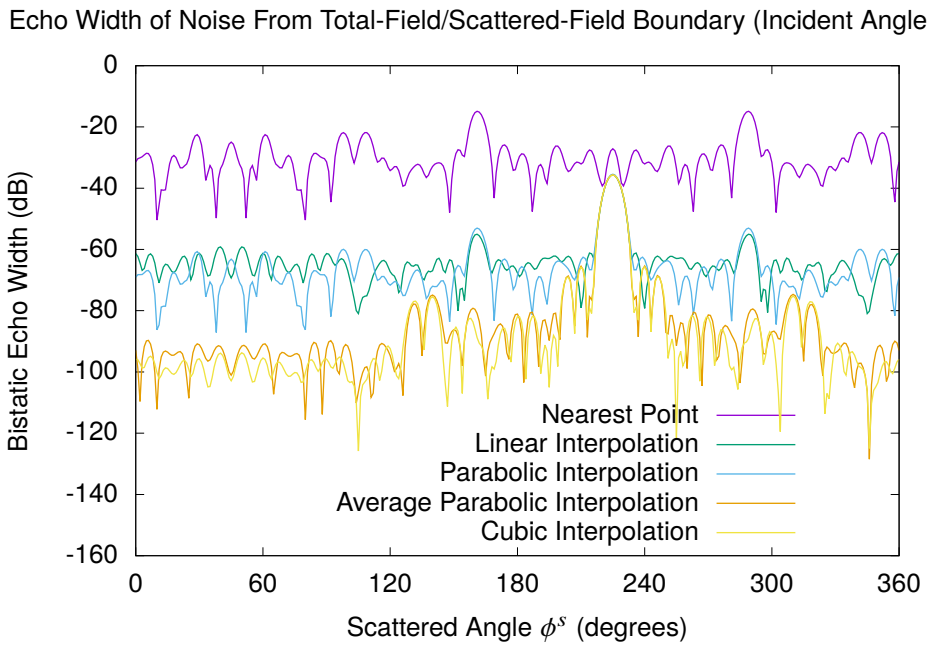

Fig. 8—Noise versus interpolation method at 300 MHz for a Yee FDTD grid with $\Delta x = 0.05$ meters, 800 time steps, a 16-cell cosine PML, 4 cells between the PML and integration surface, and 3 cells between the integration surface and the TF/SF boundary.

The effects of using the nearest point from the one-dimensional Yee FDTD grid can be seen in Figure 9a for 25 ns into the FDTD calculation when compared with the cubic interpolation shown in Figure 9b. Specifically, the TF/SF boundary is ragged in Figure 9a versus Figure 9b. Also, the trailing edge of the Gaussian pulse is distorted by noise in Figure 9a. At 50 ns the Gaussian pulse is nearly at the edge of the FDTD grid and the difference is clear between the nearest point approximation shown in Figure 10a and the cubic interpolation shown in Figure 10b. At 50 ns the differences are just barely visible between linear interpolation (Figure 11a) and parabolic interpolation (Figure 11b) versus cubic interpolation (Figure 10b), even through they are clearly visible in the echo width plot of Figure 8.

(a) Gaussian Plane Wave from TF/SF Boundary with Nearest Point Approximation for ϕ^i=45° at 25 ns

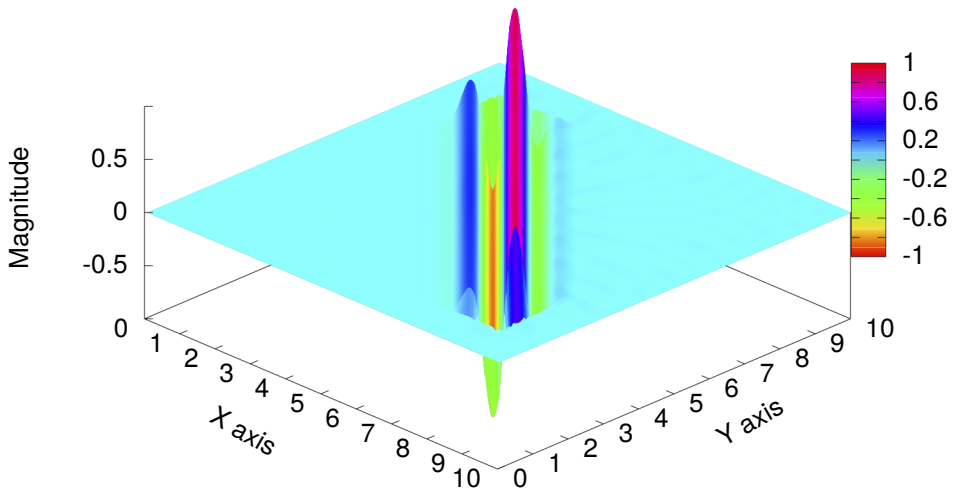

(b) Gaussian Plane Wave from TF/SF Boundary with Cubic Interpolation for ϕ^i=45° at 25 ns

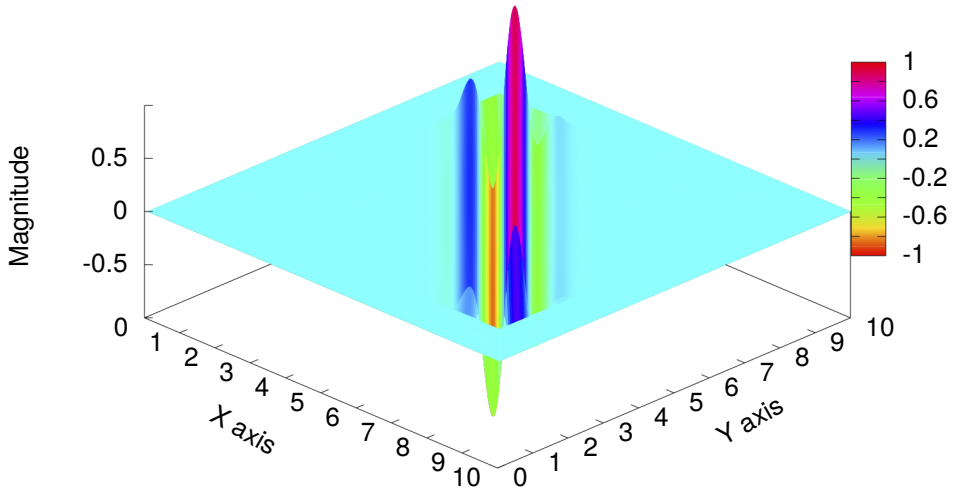

Fig. 9—Gaussian plane wave incident from $\phi^i = 45$ using TF/SF boundary excitation at 25 ns with a nearest point approximation and cubic interpolation for the one-dimensional Yee FDTD grid.

(a) Noise from TF/SF Boundary with Nearest Point Approximation for ϕ^i=45° at 50 ns

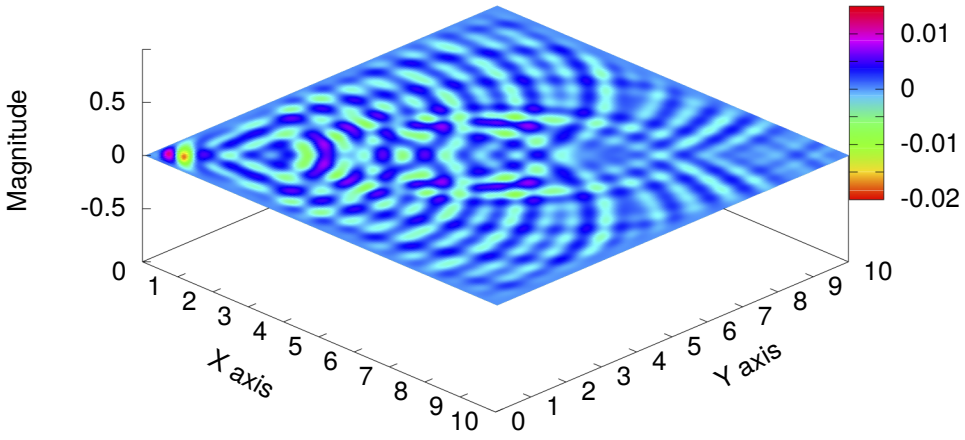

(b) Noise from TF/SF Boundary with Cubic Interpolation for ϕ^i=45° at 50 ns

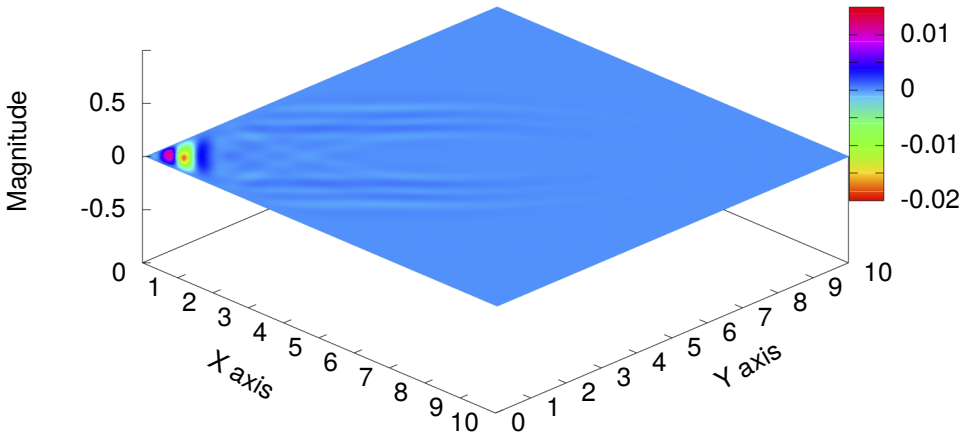

Fig. 10—Gaussian plane wave incident from ϕ^i = 45 using TF/SF boundary excitation at 50 ns with (a) nearest point approximation and (b) cubic interpolation for the one-dimensional Yee FDTD grid.

(a) Noise from TF/SF Boundary with Linear Interpolation for ϕ^i=45° at 50 ns

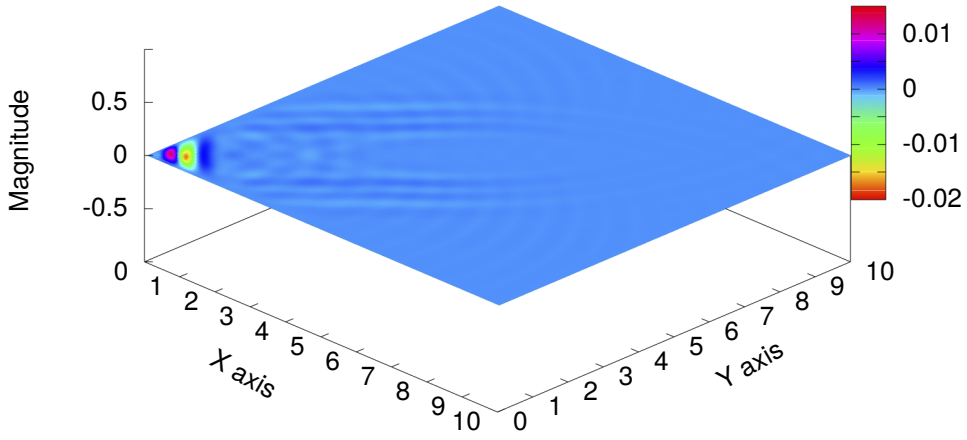

(b) Noise from TF/SF Boundary with Parabolic Interpolation for ϕ^i=45° at 50 ns

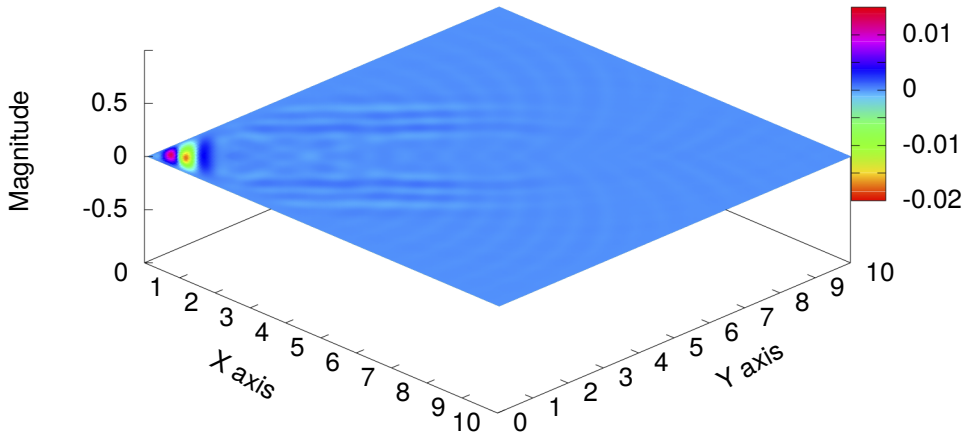

Fig. 11—Gaussian plane wave incident from ϕ^i = 45 using TF/SF boundary excitation at 50 ns with (a) linear and (b) parabolic interpolation for the one-dimensional Yee FDTD grid.

5. LOCATION OF SCATTERED FIELD INTEGRATION

The conventional approach is to maintain separation between the PML region, the scattered field integration, and the TF/SF boundary. However, as the separation increases to overall size of the FDTD grid it also increases the computation cost of the FDTD simulation. As the scattered fields needed for the calculation of echo width could be created anywhere in the total-field region, I consider in this section what happens if I place the scattered field integration at the edge of the TF/SF region. Following the definitions above the edge of total-field region consists of $\mathcal{E}_z$ fields, but since I have to calculate the incident field at these points, I effectively already have the scattered field at these points. So I linearly interpolate the scattered $\mathcal{E}_z$ fields across the TF/SF boundary and take the $\mathcal{H}_x$, $\mathcal{H}_y$ fields from the edge of the scattered field region. My first test, shown in Figure 12, is the calculation of the noise for $\phi^i = 0°$ with the same parameters as in Figure 7 but with the modified scattered field integration. These results indicate correct implementation

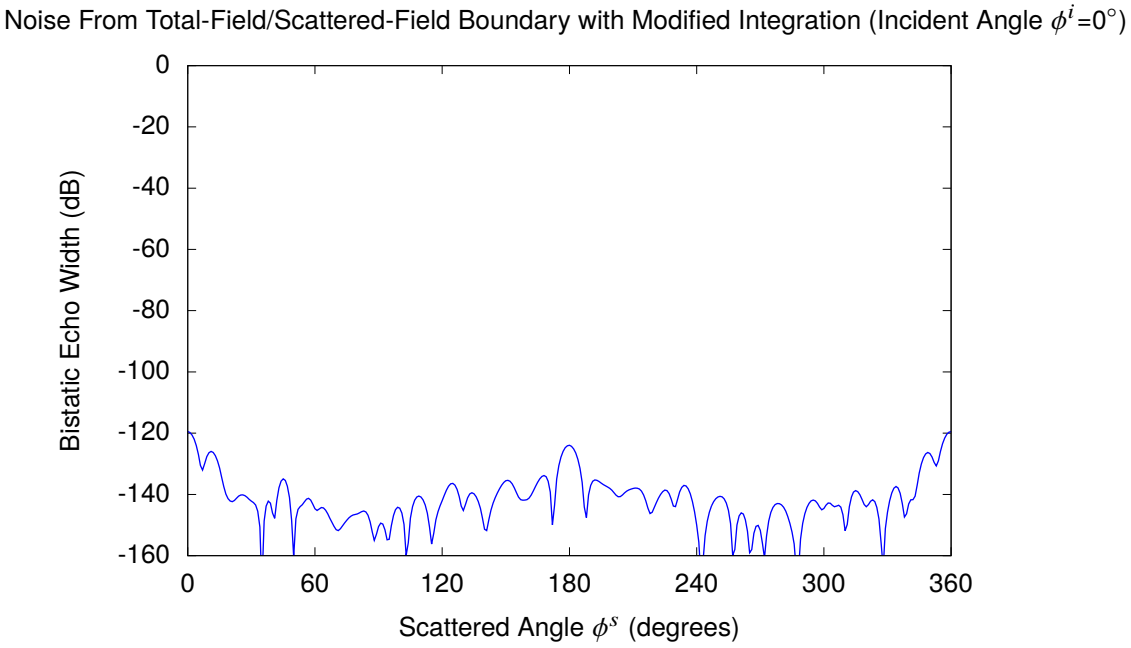

Fig. 12—Bistatic noise at 300 MHz for a Yee FDTD grid with $\Delta x = 0.05$ meters, 800 time steps, a 16-cell cosine PML, 7 cells between the PML and integration surface, with the integration surface overlapping the TF/SF boundary.

of the integration boundary and TF/SF boundary within numerical limitations. For a second test, I look at $\phi^i = 45°$ in Figure 13, and I see an increased noise floor, but not enough to prevent usage of this approach versus the advantage of reducing the number of FDTD cells between the PML region and the scatterer. However, in Figure 14 I present the echo width calculation with this modified location for the scattered field integration for the 1 meter square cylinder previously shown in Figure 5. The majority of the ripple in this calculation is caused by noise at the TF/SF boundary that does not propagate in the Yee FDTD grid but by integrating directly at the TF/SF boundary I am capturing that noise. Also, there is some noise caused by having moved the scattered field integration closer to the scatterer as the scattered fields spatially vary more rapidly the closer you are to the scatterer. This effect is reduced in Figure 15 where the scattered field integration is moved to the same location as in Figure 5 while also moving the TF/SF boundary adjacent to scattered field integration. Based on the results in this section, it is clear that the best results are obtained

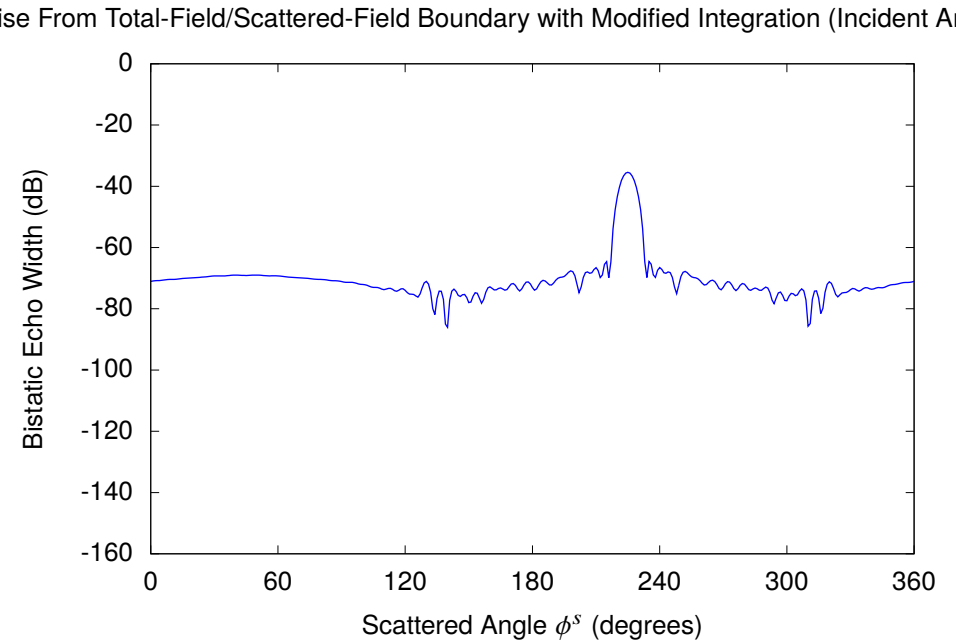

Fig. 13—Bistatic noise at 300 MHz for a Yee FDTD grid with Δx = 0.05 meters, 800 time steps, a 16-cell cosine PML, 7 cells between the PML and integration surface, with the integration surface overlapping the TF/SF boundary.

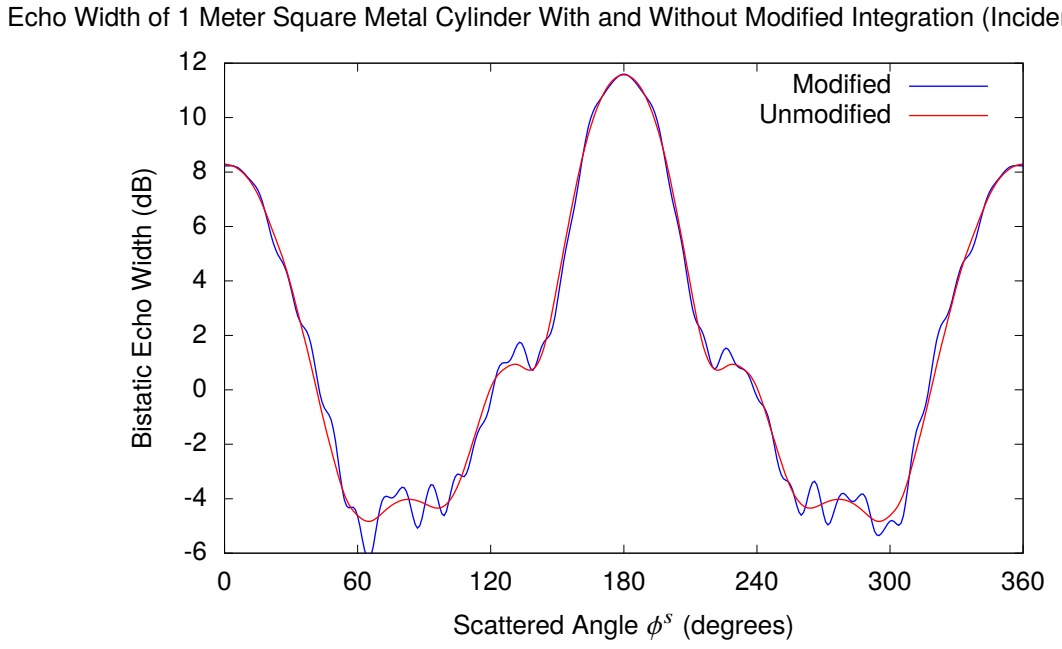

Fig. 14—Bistatic echo width of a 1 meter metal square cylinder at 300 MHz for a Yee FDTD grid with Δx = 0.05 meters, 800 time steps, a 16-cell cosine PML, 7 cells between the PML and TF/SF boundary, with the integration surface overlapping the TF/SF boundary versus 3 cell separation from TF/SF boundary.

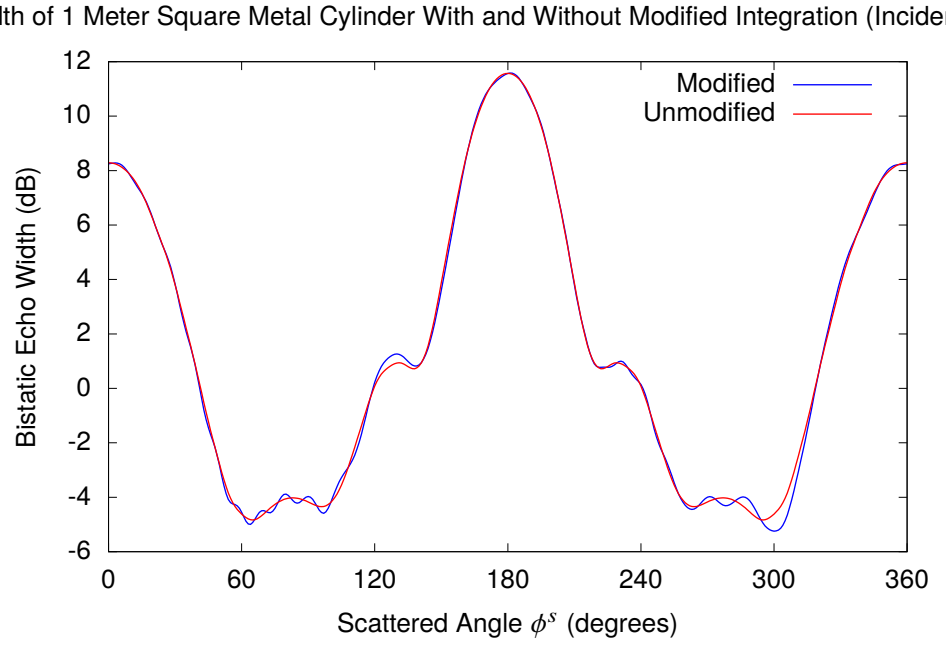

Fig. 15—Bistatic echo width of a 1 meter metal square cylinder at 300 MHz for a Yee FDTD grid with $\Delta x = 0.05$ meters, 800 time steps, a 16-cell cosine PML, 4 cells between the PML and integration surface, with the integration surface overlapping the TF/SF boundary versus 3 cell separation from TF/SF boundary.

when the separation between the TF/SF boundary and the scattered field integration is on the order of at least three cells as originally used for Figure 5.

6. REFERENCE PROBLEM FOR SCATTERED FIELD CALCULATIONS

I need a reference problem in order to evaluate the accuracy of the scattered field calculations in Yee FDTD versus advanced FDTD methods. The least complicated exact analytical two-dimensional solution is plane wave scattering from an infinite circular cylinder parallel to the z-axis. For $\phi^i = 180°$, the far-field frequency-domain scattered field is given by the eigenfunction equation

$$\frac{E_z(k_0)}{E^i(k_0)} = \sqrt{\frac{2j}{\pi k_0}} \left[\frac{J_0(k_0 a)}{H_0^{(2)}(k_0 a)} + 2 \sum_{n=0}^{\infty} \frac{J_n(k_0 a)}{H_n^{(2)}(k_0 a)} \cos(n\phi^s) \right], \tag{23}$$

where a is the radius of the cylinder, J_n is the Bessel function of the first kind of order n, and $H_n^{(2)}$ is the Hankel function of the second kind of order n [2, Section 5-9], [3, Section 11.5.1], [23, Section 2.1]. To demonstrate the convergence of the Yee FDTD, I show in Figure 16 the exact solution for a metal cylinder one meter in diameter versus a Yee FDTD calculation with $\Delta x = 0.01$ meters at 300 MHz (100 cells per wavelength). In contrast, I show in Figure 17 the same solution versus a Yee FDTD calculation with $\Delta x = 0.05$ meters at 300 MHz (20 cells per wavelength). The errors in Figure 17 are due to the staircase representation of objects in the Yee FDTD, where the fields near the surface are not well represented by a simple linear function between the FDTD points.

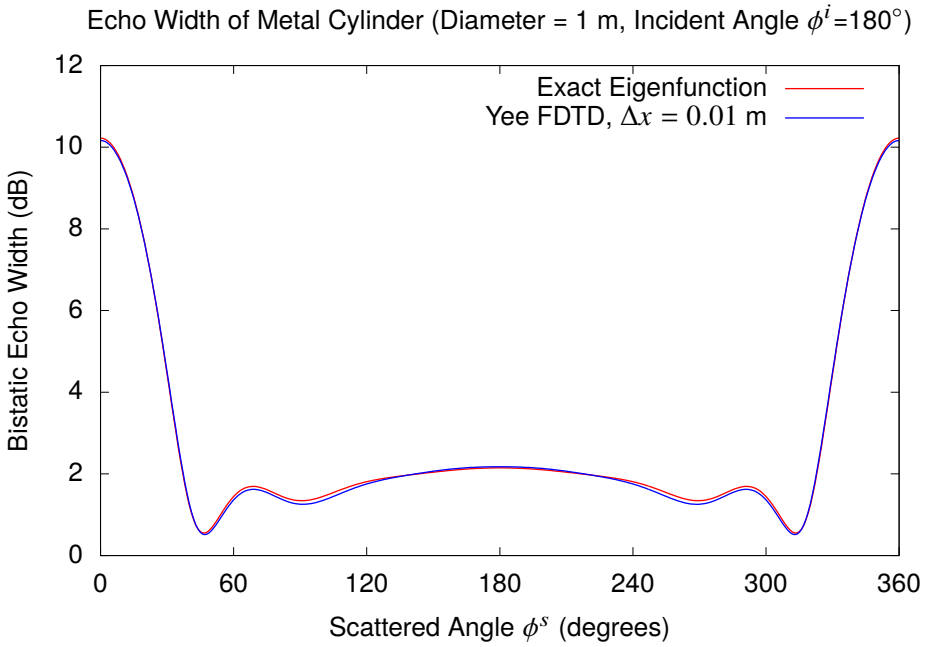

Fig. 16—Bistatic echo width of a metal cylinder one meter in diameter at 300 MHz for an exact analytic eigenfunction solution versus a Yee FDTD solution with $\Delta x = 0.01$ meters (100 cells per λ), 1720 time steps, a 16-cell cosine PML, 15 cells between the PML and the integration surface, and 30 cells between the integration surface and the TF/SF boundary.

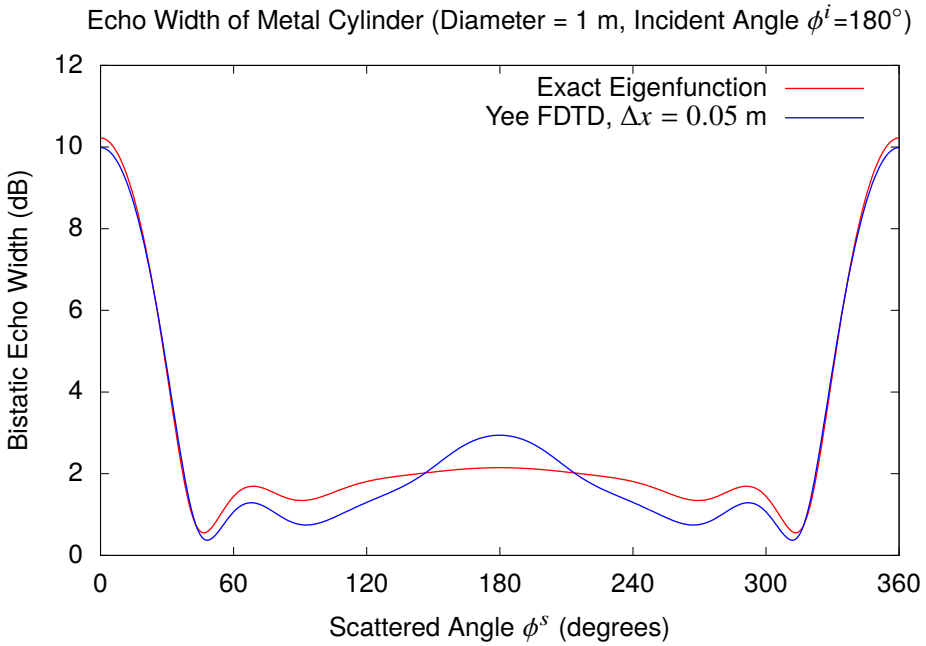

Fig. 17—Bistatic echo width of a metal cylinder one meter in diameter at 300 MHz for the exact analytic eigenfunction solution versus a Yee FDTD solution with $\Delta x = 0.05$ meters (20 cells per λ), 340 time steps, a 16-cell cosine PML, 3 cells between the PML and the integration surface, and 6 cells between the integration surface and the TF/SF boundary versus the analytic eigenfunction solution.

In order to evaluate a potential solution to the FDTD stair-casing problem, I first consider the problem of scattering from small cylinders. In Figure 18, I show the exact solution for a metal cylinder with a diameter of 0.0708 meters versus FDTD calculations with $\Delta x = 0.01$ meters and $\Delta x = 0.05$ meters at 300 MHz. The radius and position of the cylinder was picked so that four $\mathcal{E}_z$ FDTD edges in a square align with the

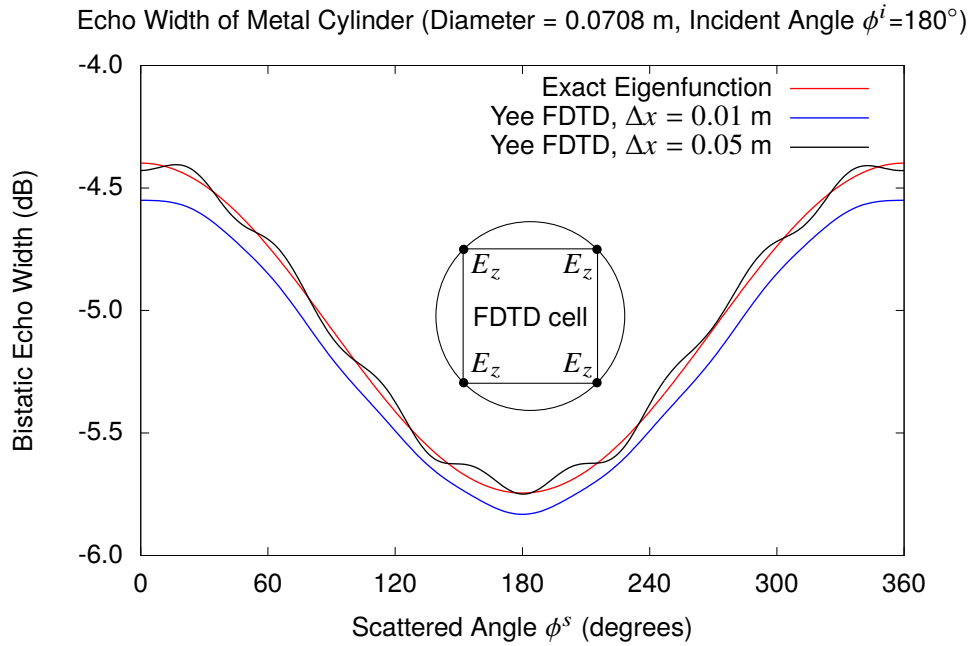

Fig. 18—Bistatic echo width of a metal cylinder 0.0708 meters in diameter at 300 MHz for the exact analytic eigenfunction solution versus Yee FDTD solutions with $\Delta x = 0.01$ and 0.05 meters.

surface of the cylinder in the $\Delta x = 0.05$ meter FDTD grid, thereby forcing the $\mathcal{E}_z$ field to zero at those four points. In this case, the $\Delta x = 0.05$ meter FDTD calculation is more accurate than the $\Delta x = 0.01$ meter FDTD calculation. However, in general this cylinder would not line up perfectly in a $\Delta x = 0.05$ meter FDTD grid and then only a single $\mathcal{E}_z$ FDTD edge would represent the cylinder resulting in a much lower scattered field. This is what happens for the smaller cylinder with a diameter of 0.05 meters shown in Figure 19. In this case the cylinder is represented by a single $\mathcal{E}_z$ FDTD edge which has a scattered field 3 dB less than the actual cylinder. Even though the cylinder is represented by 16 E_z FDTD grid points in the $\Delta x = 0.01$ meter FDTD calculation, the resulting scattered field is 1 dB less than the exact answer. Any technique that can improve the FDTD calculations for the small cylinders shown in Figures 18 – 19 has the potential to generalize to the large cylinder in Figure 17 and more complex geometries.

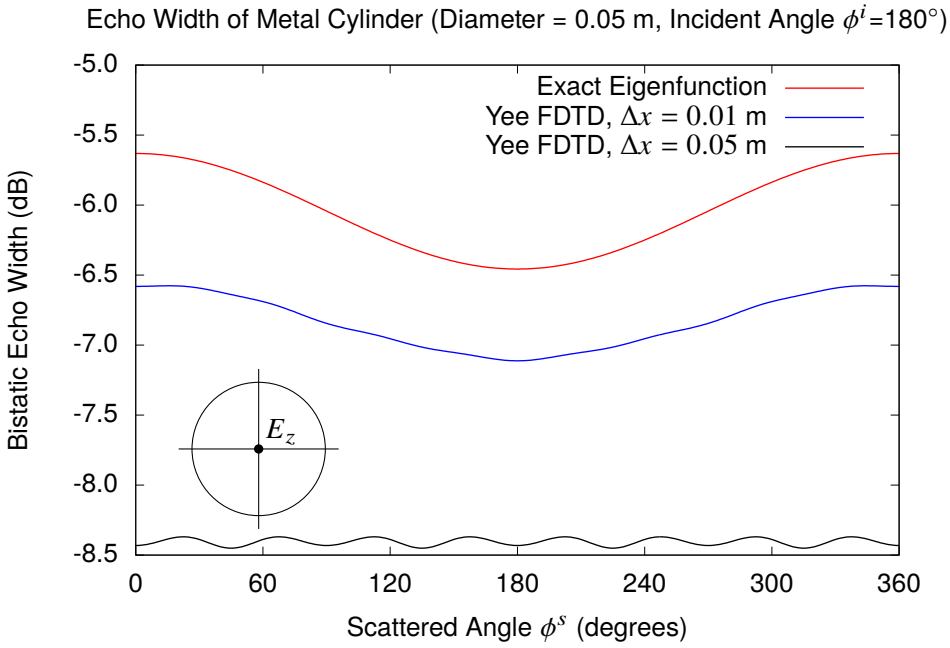

Fig. 19—Bistatic echo width of a metal cylinder 0.05 meters in diameter at 300 MHz for the exact analytic eigenfunction solution versus Yee FDTD solutions with Δx = 0.01 and 0.05 meters. The cylinder is centered on a E_z FDTD point resulting in scattering from only that point for Δx = 0.05.

7. ENHANCED FDTD TECHNIQUES

In order to increase the accuracy of Yee FDTD without drastically increasing the number of Yee FDTD cells, I need to either use a subgridding technique [24–27] where selected FDTD cells are subdivided into smaller cells or use a subcell technique to modify the FDTD equations to account for the differences in the FDTD cells at the interface between two materials. In this section, I examine a subcell technique leaving subgridding for future development. Early subcell techniques for enhancing the Yee FDTD method used the integral form of Maxwell's equations with the Yee FDTD grid while retaining the assumption of linear field variation across the FDTD cells [28–33]. This approach does not account for the field behavior near surfaces and is limited to simple surfaces cutting through a FDTD cell. Alternative approaches were developed to include knowledge about fields around small cylinders and at edges [34–36]. These techniques are often referred to as quasistatic techniques. Quasistatics refers to electromagnetic solutions that are neither electrostatic nor electrodynamic solutions. The electroquasistatics model [37] is defined by adding time-dependence to the Coulomb electric field

$$\boldsymbol{\mathcal{E}}_C(\mathbf{r},t) = \frac{1}{4\pi\epsilon_0}\iiint \frac{\rho(\mathbf{r}',t)\,\hat{\mathbf{R}}}{R^2}dv', \tag{24}$$

and the Biot-Savart law

$$\boldsymbol{\mathcal{B}}(\mathbf{r},t) = \frac{\mu_0}{4\pi}\iiint \frac{\boldsymbol{\mathcal{J}}(\mathbf{r}',t)\times\hat{\mathbf{R}}}{R^2}dv', \tag{25}$$

combined with the continuity equation

$$\nabla\cdot\boldsymbol{\mathcal{J}}(\mathbf{r},t) = -\frac{\partial\rho(\mathbf{r},t)}{\partial t}, \tag{26}$$

where Equation (24) solves the differential equations

$$\nabla\times\boldsymbol{\mathcal{E}}_C(\mathbf{r},t) = 0, \tag{27a}$$

$$\nabla\cdot\boldsymbol{\mathcal{E}}_C(\mathbf{r},t) = 0, \tag{27b}$$

with $\mathbf{R} = \bar{\mathbf{r}} - \bar{\mathbf{r}}'$, $R = |\mathbf{R}|$, and $\hat{\mathbf{R}} = \mathbf{R}/\mathbf{R}$. The Darwin quasistatic model [37] adds the Faraday electric field

$$\boldsymbol{\mathcal{E}}_F(\mathbf{r},t) = -\frac{1}{4\pi}\iiint \frac{\partial\boldsymbol{\mathcal{B}}(\mathbf{r}',t)}{\partial t}\times\frac{\hat{\mathbf{R}}}{R^2}dv', \tag{28}$$

which solves the differential equations

$$\nabla\times\boldsymbol{\mathcal{E}}_F(\mathbf{r},t) = -\frac{\partial\boldsymbol{\mathcal{B}}(\mathbf{r},t)}{\partial t}, \tag{29a}$$

$$\nabla\cdot\boldsymbol{\mathcal{E}}_F(\mathbf{r},t) = \frac{\rho(\mathbf{r},t)}{\epsilon}, \tag{29b}$$

where the total electric field is given by $\boldsymbol{\mathcal{E}}(\mathbf{r},t) = \boldsymbol{\mathcal{E}}_C(\mathbf{r},t) + \boldsymbol{\mathcal{E}}_F(\mathbf{r},t)$. The quasistatic approximations to Maxwell's equations enable approximate solutions to problems that are either very expensive or impossible

to solve exactly. Integrating the exact electric and magnetic fields near a cylinder from the eigenfunction solution is one such problem. In this section I examine the development of an enhanced FDTD technique with regards to the small cylinders in Figures 18 – 19 and evaluate this technique for the larger cylinder in Figures 16 – 17.

7.1 Modified Assigned Material Parameters

While sometimes successful, the use of known field behavior in combination with the integral form of Maxwell's equations is problematic in that stability can not be proven in general for the resulting equations. A recent development is the concept of modified assigned material parameters (MAMP) [38–42]. A correction factor to the material parameters of a cell is calculated for structures in a cell, thereby accounting for nonlinear field distributions in the cell. As this is equivalent to a physical material, the resulting FDTD equations have the same stability constraints as Yee FDTD. The development of the conformal and MAMP techniques start with the integral form of Maxwell's equations,

$$\frac{\partial}{\partial t}\iint \epsilon \boldsymbol{\mathcal{E}}(t)\cdot d\mathbf{s} + \iint \sigma \boldsymbol{\mathcal{E}}(t)\cdot d\mathbf{s} = \oint \boldsymbol{\mathcal{H}}(t)\cdot d\mathbf{l}, \tag{30a}$$

$$\frac{\partial}{\partial t}\iint \mu \boldsymbol{\mathcal{H}}(t)\cdot d\mathbf{s} + \iint \sigma^{*} \boldsymbol{\mathcal{H}}(t)\cdot d\mathbf{s} = -\oint \boldsymbol{\mathcal{E}}(t)\cdot d\mathbf{l}, \tag{30b}$$

generalized from Equations (2a) – (2b) to account for the effective conductivities [1]. For example, when applied to the three-dimensional Yee FDTD grid for $\mathcal{E}_z$, $\mathcal{H}_x$, and $\mathcal{H}_y$, I get

$$\begin{aligned}\frac{\partial}{\partial t}\int_{y-\frac{\Delta y}{2}}^{y+\frac{\Delta y}{2}}\int_{x-\frac{\Delta x}{2}}^{x+\frac{\Delta x}{2}} \epsilon\mathcal{E}_z(x',y',z+\tfrac{\Delta z}{2},t)\,dx'dy' + \int_{y-\frac{\Delta y}{2}}^{y+\frac{\Delta y}{2}}\int_{x-\frac{\Delta x}{2}}^{x+\frac{\Delta x}{2}} \sigma\mathcal{E}_z(x',y',z+\tfrac{\Delta z}{2},t)\,dx'dy' = \\ \int_{y-\frac{\Delta y}{2}}^{y+\frac{\Delta y}{2}} \mathcal{H}_y(x+\tfrac{\Delta x}{2},y',z+\tfrac{\Delta z}{2},t)dy' + \int_{x+\frac{\Delta x}{2}}^{x-\frac{\Delta x}{2}} \mathcal{H}_x(x',y+\tfrac{\Delta y}{2},z+\tfrac{\Delta z}{2},t)dx' \\ + \int_{y+\frac{\Delta y}{2}}^{y-\frac{\Delta y}{2}} \mathcal{H}_y(x-\tfrac{\Delta x}{2},y',z+\tfrac{\Delta z}{2},t)dy' + \int_{x-\frac{\Delta x}{2}}^{x+\frac{\Delta x}{2}} \mathcal{H}_x(x',y-\tfrac{\Delta y}{2},z+\tfrac{\Delta z}{2},t)dx',\end{aligned} \tag{31a}$$

$$\begin{aligned}\frac{\partial}{\partial t}\int_{z}^{z+\Delta z}\int_{y}^{y+\Delta y} \mu\mathcal{H}_x(x,y',z',t)\,dy'dz' + \int_{z}^{z+\Delta z}\int_{y}^{y+\Delta y} \sigma^{*}\mathcal{H}_x(x,y',z',t)\,dy'dz' = \\ -\int_{z}^{z+\Delta z} \mathcal{E}_z(x,y+\Delta y,z',t)dz' - \int_{y+\Delta y}^{y} \mathcal{E}_y(x,y',z+\Delta z,t)dy' \\ -\int_{z+\Delta z}^{z} \mathcal{E}_z(x,y,z',t)dz' - \int_{y}^{y+\Delta y} \mathcal{E}_y(x,y',z,t)dy',\end{aligned} \tag{31b}$$

$$\frac{\partial}{\partial t}\int_z^{z+\Delta z}\int_x^{x+\Delta x}\mu\mathcal{H}_y(x',y,z',t)\,dx'dz' + \int_z^{z+\Delta z}\int_x^{x+\Delta x}\sigma^*\mathcal{H}_y(x',y,z',t)\,dx'dz' =$$
$$-\int_z^{z+\Delta z}\mathcal{E}_z(x,y,z',t)dz' - \int_x^{x+\Delta x}\mathcal{E}_x(x',y,z+\Delta z,t)dx'$$
$$-\int_{z+\Delta z}^{z}\mathcal{E}_z(x+\Delta x,y,z',t)dz' - \int_{x+\Delta x}^{x}\mathcal{E}_x(x',y,z,t)dx', \quad (31c)$$

where the geometry for Equations (31a) – (31b) is shown in Figure 20. If I assume the electric and

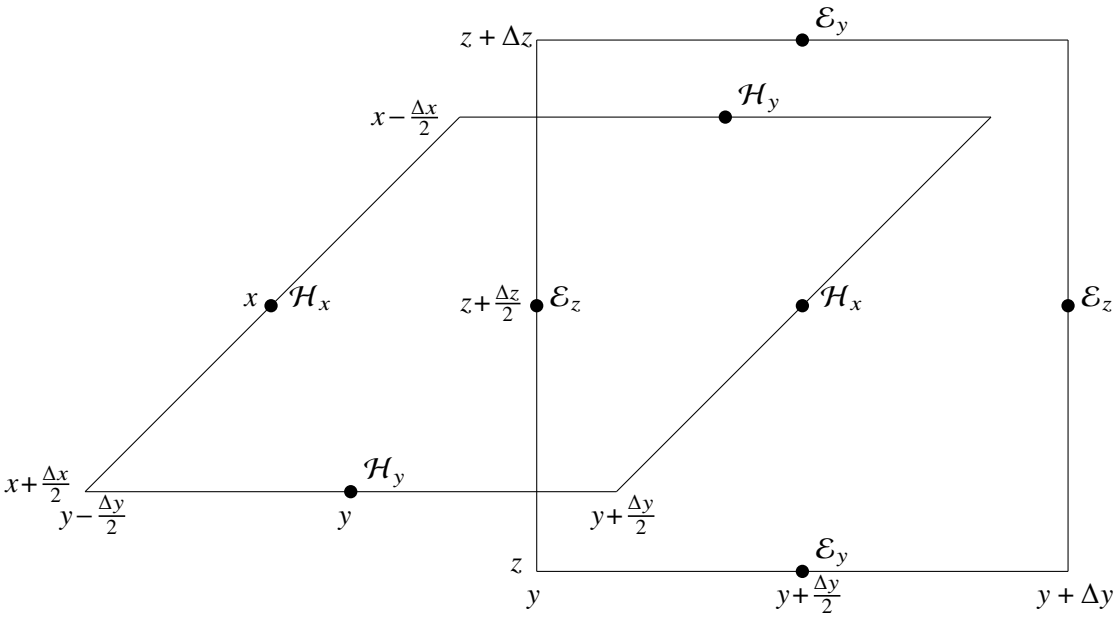

Fig. 20—$\mathcal{E}_z$ and $\mathcal{H}_x$ Integration contours for the Yee FDTD grid.

magnetic fields in Equation (31) are linear functions of x, y, and z, I get the Yee FDTD update equations for $\mathcal{E}_z$, $\mathcal{H}_x$, and $\mathcal{H}_y$ before the time derivative is approximated (Equations 22c, 23a, and 23b from [1])

$$\Delta x\Delta y\left(\frac{\partial}{\partial t}\epsilon+\sigma\right)\mathcal{E}_z(x,y,z+\tfrac{\Delta z}{2},t) = \Delta y\left(\mathcal{H}_y(x+\tfrac{\Delta x}{2},y,z+\tfrac{\Delta z}{2},t)-\mathcal{H}_y(x-\tfrac{\Delta x}{2},y,z+\tfrac{\Delta z}{2},t)\right)$$
$$-\Delta x\left(\mathcal{H}_x(x,y+\tfrac{\Delta y}{2},z+\tfrac{\Delta z}{2},t)-\mathcal{H}_x(x,y-\tfrac{\Delta y}{2},z+\tfrac{\Delta z}{2},t)\right), \quad (32a)$$

$$\Delta y\Delta z\left(\frac{\partial}{\partial t}\mu+\sigma^*\right)\mathcal{H}_x(x,y+\tfrac{\Delta y}{2},z+\tfrac{\Delta z}{2},t) = -\Delta z\left(\mathcal{E}_z(x,y+\Delta y,z+\tfrac{\Delta z}{2},t)-\mathcal{E}_z(x,y,z+\tfrac{\Delta z}{2},t)\right)$$
$$+\Delta y\left(\mathcal{E}_y(x,y+\tfrac{\Delta y}{2},z+\Delta z,t)-\mathcal{E}_y(x,y+\tfrac{\Delta y}{2},z,t)\right). \quad (32b)$$

$$\Delta x\Delta z\left(\frac{\partial}{\partial t}\mu+\sigma^*\right)\mathcal{H}_y(x+\tfrac{\Delta x}{2},y,z+\tfrac{\Delta z}{2},t) = \Delta z\left(\mathcal{E}_z(x+\Delta x,y,z+\tfrac{\Delta z}{2},t)-\mathcal{E}_z(x,y,z+\tfrac{\Delta z}{2},t)\right)$$
$$-\Delta x\left(\mathcal{E}_x(x+\tfrac{\Delta x}{2},y,z+\Delta z,t)-\mathcal{E}_x(x+\tfrac{\Delta x}{2},y,z,t)\right). \quad (32c)$$

A significant approximation in Yee FDTD is the implicit assumption that

$$\frac{1}{\Delta x \Delta y}\int_{y-\frac{\Delta y}{2}}^{y+\frac{\Delta y}{2}}\int_{x-\frac{\Delta x}{2}}^{x+\frac{\Delta x}{2}} \mathcal{E}_z(x',y',z+\tfrac{\Delta z}{2},t)\,dx'dy' = \frac{1}{\Delta z}\int_{z}^{z+\Delta z} \mathcal{E}_z(x,y,z',t)dz', \tag{33a}$$

$$\frac{1}{\Delta y \Delta z}\int_{z}^{z+\Delta z}\int_{y}^{y+\Delta y} \mathcal{H}_x(x,y',z',t)\,dy'dz' = \frac{1}{\Delta x}\int_{x-\frac{\Delta x}{2}}^{x+\frac{\Delta x}{2}} \mathcal{H}_x(x',y+\tfrac{\Delta y}{2},z+\tfrac{\Delta z}{2},t)dx', \tag{33b}$$

$$\frac{1}{\Delta x \Delta z}\int_{z}^{z+\Delta z}\int_{x}^{x+\Delta x} \mathcal{H}_y(x',y,z',t)\,dx'dz' = \frac{1}{\Delta y}\int_{y-\frac{\Delta y}{2}}^{y+\frac{\Delta y}{2}} \mathcal{H}_y(x+\tfrac{\Delta x}{2},y',z+\tfrac{\Delta z}{2},t)dy', \tag{33c}$$

which is not apparent in the derivation via finite difference approximations to Maxwell's differential equations, which themselves are also are not valid at material discontinuities. Following and expanding on the development of MAMP from [39, 41, 42], I first restructure Equation (31) such that

$$\left(\frac{\partial}{\partial t}+\frac{\sigma}{\epsilon}\right)\int_{y-\frac{\Delta y}{2}}^{y+\frac{\Delta y}{2}}\int_{x-\frac{\Delta x}{2}}^{x+\frac{\Delta x}{2}} \mathcal{E}_z(x',y',z+\tfrac{\Delta z}{2},t)\,dx'dy' =$$
$$\frac{1}{\epsilon}\left(\int_{y-\frac{\Delta y}{2}}^{y+\frac{\Delta y}{2}} \mathcal{H}_y(x+\tfrac{\Delta x}{2},y',z+\tfrac{\Delta z}{2},t)\,dy' - \int_{y-\frac{\Delta y}{2}}^{y+\frac{\Delta y}{2}} \mathcal{H}_y(x-\tfrac{\Delta x}{2},y',z+\tfrac{\Delta z}{2},t)\,dy'\right.$$
$$\left. - \int_{x-\frac{\Delta x}{2}}^{x+\frac{\Delta x}{2}} \mathcal{H}_x(x',y+\tfrac{\Delta y}{2},z+\tfrac{\Delta z}{2},t)\,dx' + \int_{x-\frac{\Delta x}{2}}^{x+\frac{\Delta x}{2}} \mathcal{H}_x(x',y-\tfrac{\Delta y}{2},z+\tfrac{\Delta z}{2},t)\,dx'\right), \tag{34a}$$

$$\left(\frac{\partial}{\partial t}+\frac{\sigma^*}{\mu}\right)\int_{z}^{z+\Delta z}\int_{y}^{y+\Delta y} \mathcal{H}_x(x,y',z',t)\,dy'dz' =$$
$$\frac{1}{\mu}\left(-\int_{z}^{z+\Delta z} \mathcal{E}_z(x,y+\Delta y,z',t)\,dz' + \int_{z}^{z+\Delta z} \mathcal{E}_z(x,y,z',t)\,dz'\right.$$
$$\left. + \int_{y}^{y+\Delta y} \mathcal{E}_y(x,y',z+\Delta z,t)\,dy' - \int_{y}^{y+\Delta y} \mathcal{E}_y(x,y',z,t)\,dy'\right), \tag{34b}$$

$$\left(\frac{\partial}{\partial t}+\frac{\sigma^*}{\mu}\right)\int_{z}^{z+\Delta z}\int_{x}^{x+\Delta x} \mathcal{H}_y(x',y,z',t)\,dx'dz' =$$
$$\frac{1}{\mu}\left(\int_{z}^{z+\Delta z} \mathcal{E}_z(x+\Delta x,y,z',t)\,dz' - \int_{z}^{z+\Delta z} \mathcal{E}_z(x,y,z',t)\,dz'\right.$$
$$\left. - \int_{x}^{x+\Delta x} \mathcal{E}_x(x',y,z+\Delta z,t)\,dx' + \int_{x}^{x+\Delta x} \mathcal{E}_x(x',y,z,t)\,dx'\right), \tag{34c}$$

where I have transposed all the line integrals into an identical format. Next I restructure Equation (34) to

$$\left(\frac{\partial}{\partial t}+\frac{\sigma}{\epsilon}\right)\int_{z}^{z+\Delta z}\mathcal{E}_z(x,y,z',t)dz' = \frac{1}{\epsilon_z(x,y,z+\frac{\Delta z}{2})\epsilon}\left(\int_{y-\frac{\Delta y}{2}}^{y+\frac{\Delta y}{2}}\mathcal{H}_y(x+\tfrac{\Delta x}{2},y',z+\tfrac{\Delta z}{2},t)dy' - \int_{y-\frac{\Delta y}{2}}^{y+\frac{\Delta y}{2}}\mathcal{H}_y(x-\tfrac{\Delta x}{2},y',z+\tfrac{\Delta z}{2},t)dy' - \int_{x-\frac{\Delta x}{2}}^{x+\frac{\Delta x}{2}}\mathcal{H}_x(x',y+\tfrac{\Delta y}{2},z+\tfrac{\Delta z}{2},t)dx' + \int_{x-\frac{\Delta x}{2}}^{x+\frac{\Delta x}{2}}\mathcal{H}_x(x',y-\tfrac{\Delta y}{2},z+\tfrac{\Delta z}{2},t)dx'\right), \quad (35a)$$

$$\left(\frac{\partial}{\partial t}+\frac{\sigma*}{\mu}\right)\int_{x-\frac{\Delta x}{2}}^{x+\frac{\Delta x}{2}}\mathcal{H}_x(x',y+\tfrac{\Delta y}{2},z+\tfrac{\Delta z}{2},t)dx' = \frac{1}{\mu_x(x,y+\frac{\Delta y}{2},z+\frac{\Delta z}{2})\mu}\left(-\int_{z}^{z+\Delta z}\mathcal{E}_z(x,y+\Delta y,z',t)dz' + \int_{z}^{z+\Delta z}\mathcal{E}_z(x,y,z',t)dz' + \int_{y}^{y+\Delta y}\mathcal{E}_y(x,y',z+\Delta z,t)dy' - \int_{y}^{y+\Delta y}\mathcal{E}_y(x,y',z,t)dy'\right), \quad (35b)$$

$$\left(\frac{\partial}{\partial t}+\frac{\sigma^*}{\mu}\right)\int_{y-\frac{\Delta y}{2}}^{y+\frac{\Delta y}{2}}\mathcal{H}_y(x+\tfrac{\Delta x}{2},y',z+\tfrac{\Delta z}{2},t)dy' = \frac{1}{\mu_y(x+\frac{\Delta x}{2},y,z+\frac{\Delta z}{2})\mu}\left(\int_{z}^{z+\Delta z}\mathcal{E}_z(x+\Delta x,y,z',t)\,dz' - \int_{z}^{z+\Delta z}\mathcal{E}_z(x,y,z',t)\,dz' - \int_{x}^{x+\Delta x}\mathcal{E}_x(x',y,z+\Delta z,t)\,dx' + \int_{x}^{x+\Delta x}\mathcal{E}_x(x',y,z,t)\,dx'\right), \quad (35c)$$

where the correction factors for all update equations are given by

$$\epsilon_x(x+\tfrac{\Delta x}{2},y,z) = \frac{\int_{z-\frac{\Delta z}{2}}^{z+\frac{\Delta z}{2}}\int_{y-\frac{\Delta y}{2}}^{y+\frac{\Delta y}{2}}\mathcal{E}_x(x+\frac{\Delta x}{2},y',z')\,dy'dz'}{\int_{x}^{x+\Delta x}\mathcal{E}_x(x',y,z)dx'}, \quad (36a)$$

$$\epsilon_y(x,y+\tfrac{\Delta y}{2},z) = \frac{\int_{z-\frac{\Delta z}{2}}^{z+\frac{\Delta z}{2}}\int_{x-\frac{\Delta x}{2}}^{x+\frac{\Delta x}{2}}\mathcal{E}_y(x',y+\frac{\Delta y}{2},z')\,dx'dz'}{\int_{y}^{y+\Delta y}\mathcal{E}_y(x,y',z)dy'}, \quad (36b)$$

$$\epsilon_z(x,y,z+\tfrac{\Delta z}{2}) = \frac{\int_{y-\frac{\Delta y}{2}}^{y+\frac{\Delta y}{2}}\int_{x-\frac{\Delta x}{2}}^{x+\frac{\Delta x}{2}}\mathcal{E}_z(x',y',z+\frac{\Delta z}{2})\,dx'dy'}{\int_{z}^{z+\Delta z}\mathcal{E}_z(x,y,z')dz'}, \quad (36c)$$

$$\mu_x(x,y+\tfrac{\Delta y}{2},z+\tfrac{\Delta z}{2}) = \frac{\int_{z}^{z+\Delta z}\int_{y}^{y+\Delta y}\mathcal{H}_x(x,y',z')\,dy'dz'}{\int_{x-\frac{\Delta x}{2}}^{x+\frac{\Delta x}{2}}\mathcal{H}_x(x',y+\frac{\Delta y}{2},z+\frac{\Delta z}{2})dx'}, \quad (36d)$$

$$\mu_y(x+\tfrac{\Delta x}{2},y,z+\tfrac{\Delta z}{2}) = \frac{\int_{z}^{z+\Delta z}\int_{x}^{x+\Delta x}\mathcal{H}_y(x',y,z')\,dx'dz'}{\int_{y-\frac{\Delta y}{2}}^{y+\frac{\Delta y}{2}}\mathcal{H}_y(x+\frac{\Delta x}{2},y',z+\frac{\Delta z}{2})dy'}, \quad (36e)$$

$$\mu_z(x+\tfrac{\Delta x}{2}, y+\tfrac{\Delta y}{2}, z) = \frac{\int_y^{y+\Delta y}\int_x^{x+\Delta x} \mathcal{H}_z(x', y', z)\, dx'dy'}{\int_{z-\frac{\Delta z}{2}}^{z+\frac{\Delta z}{2}} \mathcal{H}_z(x+\frac{\Delta x}{2}, y+\frac{\Delta y}{2}, z')dz'}. \tag{36f}$$

I have removed the time-dependence from $\mathcal{E}$ and $\mathcal{H}$ to indicate that the fields in these equations are the characteristic time-independent fields in the FDTD cell dependent on the geometry. For a two-dimensional problem with $\mathcal{E}_z$, $\mathcal{H}_x$, and $\mathcal{H}_y$, I reduce the expanded MAMP equations, Equation (35) and Equation (36), to the following,

$$\left(\frac{\partial}{\partial t} + \frac{\sigma}{\epsilon}\right)\mathcal{E}_z(x,y,t) = \frac{1}{\epsilon_z(x,y)\epsilon}\left[\int_{y-\frac{\Delta y}{2}}^{y+\frac{\Delta y}{2}} \mathcal{H}_y(x+\tfrac{\Delta x}{2}, y', t)dy' - \int_{y-\frac{\Delta y}{2}}^{y+\frac{\Delta y}{2}} \mathcal{H}_y(x-\tfrac{\Delta x}{2}, y', t)dy' \right.$$
$$\left. - \int_{x-\frac{\Delta x}{2}}^{x+\frac{\Delta x}{2}} \mathcal{H}_x(x', y+\tfrac{\Delta y}{2}, t)dx' + \int_{x-\frac{\Delta x}{2}}^{x+\frac{\Delta x}{2}} \mathcal{H}_x(x', y-\tfrac{\Delta y}{2}, t)dx'\right], \tag{37a}$$

$$\left(\frac{\partial}{\partial t} + \frac{\sigma*}{\mu}\right)\int_{x-\frac{\Delta x}{2}}^{x+\frac{\Delta x}{2}} \mathcal{H}_x(x', y+\tfrac{\Delta y}{2}, t)dx' = \frac{1}{\mu_x(x, y+\frac{\Delta y}{2})\mu}\left[-\mathcal{E}_z(x, y+\Delta y, t) + \mathcal{E}_z(x,y,t)\right], \tag{37b}$$

$$\left(\frac{\partial}{\partial t} + \frac{\sigma^*}{\mu}\right)\int_{y-\frac{\Delta y}{2}}^{y+\frac{\Delta y}{2}} \mathcal{H}_y(x+\tfrac{\Delta x}{2}, y', t)dy' = \frac{1}{\mu_y(x+\frac{\Delta x}{2}, y)\mu}\left[\mathcal{E}_z(x+\Delta x, y, t) - \mathcal{E}_z(x,y,t)\right], \tag{37c}$$

with the following reduced correction factors

$$\epsilon_z(x,y) = \frac{\int_{y-\frac{\Delta y}{2}}^{y+\frac{\Delta y}{2}}\int_{x-\frac{\Delta x}{2}}^{x+\frac{\Delta x}{2}} \mathcal{E}_z(x', y')\, dx'dy'}{\mathcal{E}_z(x,y)}, \tag{38a}$$

$$\mu_x(x, y+\tfrac{\Delta y}{2}) = \frac{\int_y^{y+\Delta y} \mathcal{H}_x(x, y')\, dy'}{\int_{x-\frac{\Delta x}{2}}^{x+\frac{\Delta x}{2}} \mathcal{H}_x(x', y+\frac{\Delta y}{2})dx'}, \tag{38b}$$

$$\mu_y(x+\tfrac{\Delta x}{2}, y) = \frac{\int_x^{x+\Delta x} \mathcal{H}_y(x', y)\, dx'}{\int_{y-\frac{\Delta y}{2}}^{y+\frac{\Delta y}{2}} \mathcal{H}_y(x+\frac{\Delta x}{2}, y')dy'}. \tag{38c}$$

The application of MAMP to the FDTD update equations results in the slightly different FDTD parameters shown here

$$c_a = \frac{2\epsilon - \sigma\Delta t}{2\epsilon + \sigma\Delta t}, \tag{39a}$$

$$c_b = \frac{1}{\epsilon_{xyz}}\frac{2\Delta t}{2\epsilon + \sigma\Delta t}, \tag{39b}$$

$$d_a = \frac{2\mu - \sigma^*\Delta t}{2\mu + \sigma^*\Delta t}, \tag{39c}$$

$$d_b = \frac{1}{\mu_{xyz}}\frac{2\Delta t}{2\mu + \sigma^*\Delta t}. \tag{39d}$$

In a lossless material the application of the MAMP concept effectively changes the material's permittivity and permeability; however, that is not true in general as seen in Equation (39) where I can see that the coefficients indirectly modify the permittivity and permeability for the c_b and d_b parameters, but do not modify the c_a and d_a parameters.

7.2 Characteristic Near Field of Metal Cylinder

In this section I present the exact and approximate fields near a metal cylinder to develop the coefficients for the MAMP concept. From the exact analytical eigenfunction solution [2, Section 5-9], [3, Section 11.5.1] I combine terms for the electric and magnetic fields around a metal cylinder of radius a to get

$$E_z = \left[J_0(k_0\rho) + a_0 H_0^{(2)}(k_0\rho)\right] + 2\sum_{n=1}^{+\infty} j^{-n}\left[J_n(k_0\rho) + a_n H_n^{(2)}(k_0\rho)\right]\cos(n\phi), \tag{40a}$$

$$H_\rho = -\frac{2}{jk_0 c\mu_0\rho}\sum_{n=1}^{+\infty} n j^{-n}\left[J_n(k_0\rho) + a_n H_n^{(2)}(k_0\rho)\right]\sin(n\phi), \tag{40b}$$

$$H_\phi = \frac{1}{jc\mu_0}\left\{\left[J_0'(k_0\rho) + a_0 H_0^{(2)\prime}(k_0\rho)\right] + 2\sum_{n=1}^{+\infty} j^{-n}\left[J_n'(k_0\rho) + a_n H_n^{(2)\prime}(k_0\rho)\right]\cos(n\phi)\right\}, \tag{40c}$$

where $a_n = -J_n(k_0a)/H_n^{(2)}(k_0a)$ and the incident field is a unit amplitude plane wave propagating in the $+x$ direction ($\phi_i = 180°$). For small cylinders, that is $k_0a < 1$, the exact solution is dominated by the $n = 0$ term of Equation (40). Then using the derivative relationships for Bessel functions,

$$J_0'(x) = -J_1(x), \tag{41a}$$

$$H_0^{(2)\prime}(x) = -H_1^{(2)}(x), \tag{41b}$$

I approximate the fields for small cylinders as

$$E_z \approx J_0(k_0\rho) - \frac{J_0(k_0a)}{H_0^{(2)}(k_0a)} H_0^{(2)}(k_0\rho), \tag{42a}$$

$$H_\rho \approx 0, \tag{42b}$$

$$H_\phi \approx -\frac{1}{jc\mu_0}\left[J_1(k_0\rho) - \frac{J_0(k_0a)}{H_0^{(2)}(k_0a)} H_1^{(2)}(k_0\rho)\right]. \tag{42c}$$

For $k_0\rho < 1$, I approximate Equation (42) with the small argument formulas for Bessel functions [2, Appendix D], [3, Appendix IV], [43, Section 9.1],

$$J_0(x) \approx 1, \tag{43a}$$

$$Y_0(x) \approx \frac{2}{\pi}\ln\left(\frac{\gamma x}{2}\right), \tag{43b}$$

$$J_1(x) \approx \frac{x}{2}, \tag{43c}$$

$$Y_1(x) \approx -\frac{2}{\pi x}, \tag{43d}$$

where $\gamma \approx 1.781$, $H_n^{(2)}(x) = J_n(x) - jY_n(x)$, and $Y_n(x)$ is the Bessel function of the second kind of order n. With these approximations I reduce the approximate fields to

$$E_z \approx 1 - \frac{1 - j\frac{2}{\pi}\ln\left(\frac{\gamma}{2}k_0\rho\right)}{1 - j\frac{2}{\pi}\ln\left(\frac{\gamma}{2}k_0 a\right)}, \tag{44a}$$

$$H_\phi \approx -\frac{1}{jc\mu_0}\left[\frac{k_0\rho}{2} - \frac{1}{1 - j\frac{2}{\pi}\ln\left(\frac{\gamma}{2}k_0 a\right)}\left(\frac{k_0\rho}{2} + j\frac{2}{\pi k_0\rho}\right)\right]. \tag{44b}$$

To get the characteristic fields near a small cylinder, I approximate Equation (44) for $k_0 \to 0$ (a quasistatic approximation) as

$$E_z \approx 1 - \frac{\ln\left(\frac{\gamma}{2}k_0\rho\right)}{\ln\left(\frac{\gamma}{2}k_0 a\right)} = \frac{\ln\left(\frac{a}{\rho}\right)}{\ln\left(\frac{\gamma}{2}k_0 a\right)}, \tag{45a}$$

$$H_\phi \approx \frac{j}{c\mu_0 k_0 \ln\left(\frac{\gamma}{2}k_0 a\right)}\frac{1}{\rho}. \tag{45b}$$

Converting Equation (45) to rectangular coordinates I get

$$E_z \approx \frac{\ln\left(\frac{a}{\sqrt{x^2+y^2}}\right)}{\ln\left(\frac{\gamma}{2}k_0 a\right)}, \tag{46a}$$

$$H_x \approx -\frac{j}{c\mu_0 k_0 \ln\left(\frac{\gamma}{2}k_0 a\right)}\frac{y}{x^2+y^2}, \tag{46b}$$

$$H_y \approx \frac{j}{c\mu_0 k_0 \ln\left(\frac{\gamma}{2}k_0 a\right)}\frac{x}{x^2+y^2}. \tag{46c}$$

From Equation (46) I can see that except for the constant $\ln\left(\frac{\gamma}{2}k_0 a\right)$ the fields near a small cylinder are nearly independent of frequency. To evaluate these approximations for the fields near a small cylinder I first look at the metal cylinder with a diameter of 0.05 meters from Figure 19. In this case I am interested in the E_z, H_x, H_y fields in the four FDTD cells around the cylinder for $\Delta x = 0.05$ meters as shown in Figures 21 – 23. In Figure 21 I can see a correlation between the shape of the exact and approximate E_z fields. Since the approximate fields do not directly account for the incident field they do not have the directional bias seen in the exact fields. The correlation between the exact and approximate H_x fields is very strong in Figure 22, without much directional bias in the exact fields. In contrast, in Figure 23 I see a very strong directional bias in the exact H_y fields; however, the shape correlation is very strong between the exact and the approximate fields.

(a) Exact E_z Fields Near Metal Cylinder (Diameter = 0.05 m, Incident Angle ϕ^i=180°)

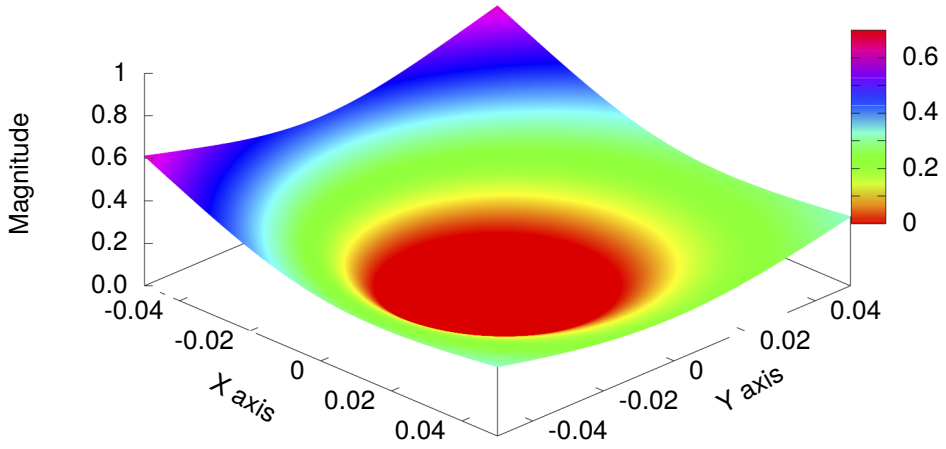

(b) Approximate E_z Fields Near Metal Cylinder (Diameter = 0.05 m)

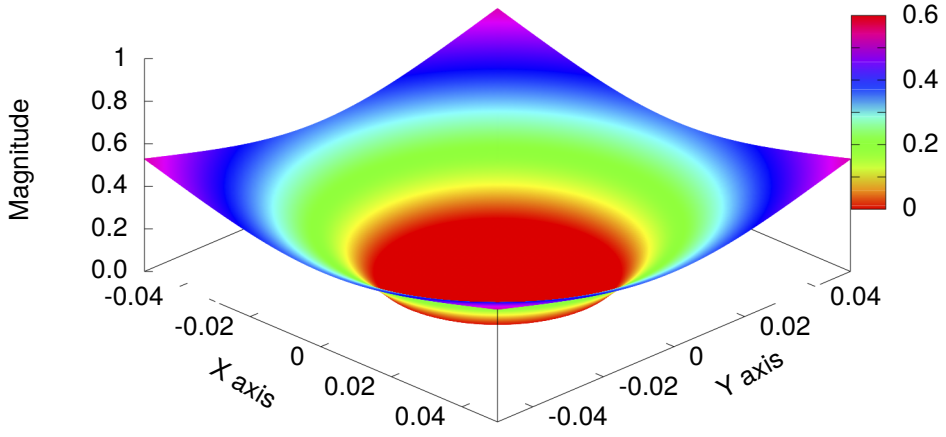

Fig. 21—Exact and approximate E_z fields near a metal cylinder 0.05 meters in diameter at 300 MHz for ϕ^i = 180.

(a) Exact H_x Fields Near Metal Cylinder (Diameter = 0.05 m, Incident Angle ϕ^i=180°)

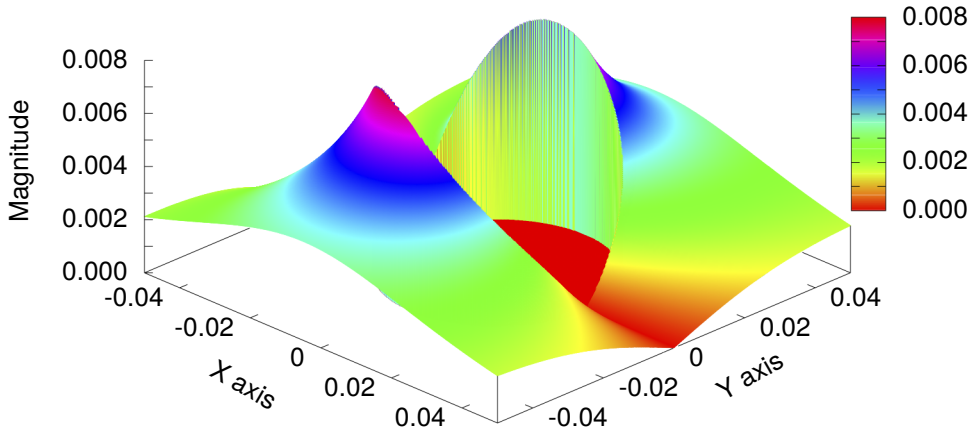

(b) Approximate H_x Fields Near Metal Cylinder (Diameter = 0.05 m)

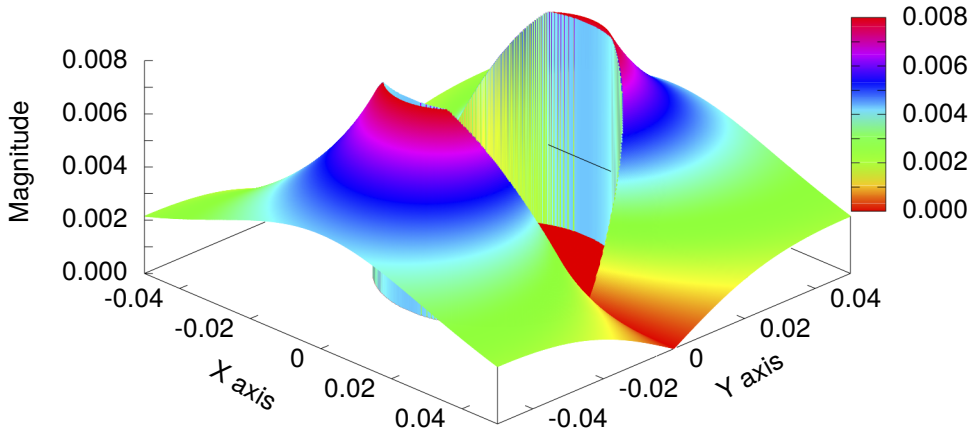

Fig. 22—Exact and approximate H_x fields near a metal cylinder 0.05 meters in diameter at 300 MHz for ϕ^i = 180.

(a) Exact H_y Fields Near Metal Cylinder (Diameter = 0.05 m, Incident Angle ϕ^i=180°)

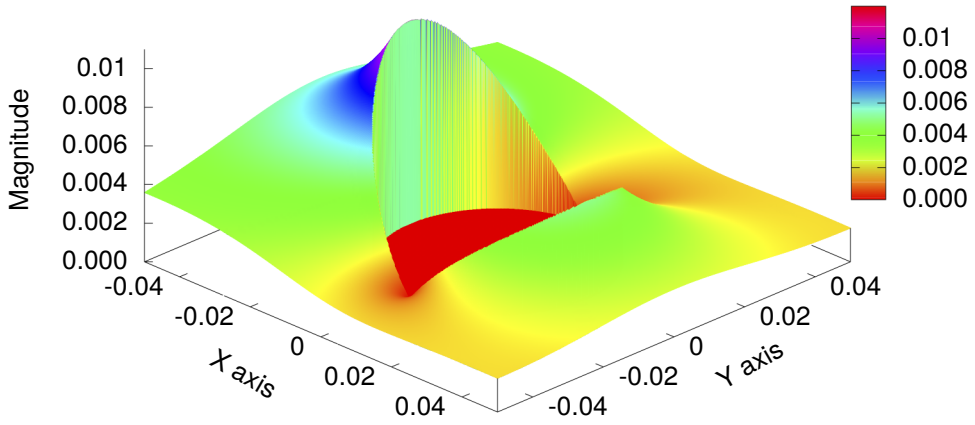

(b) Approximate H_y Fields Near Metal Cylinder (Diameter = 0.05 m)

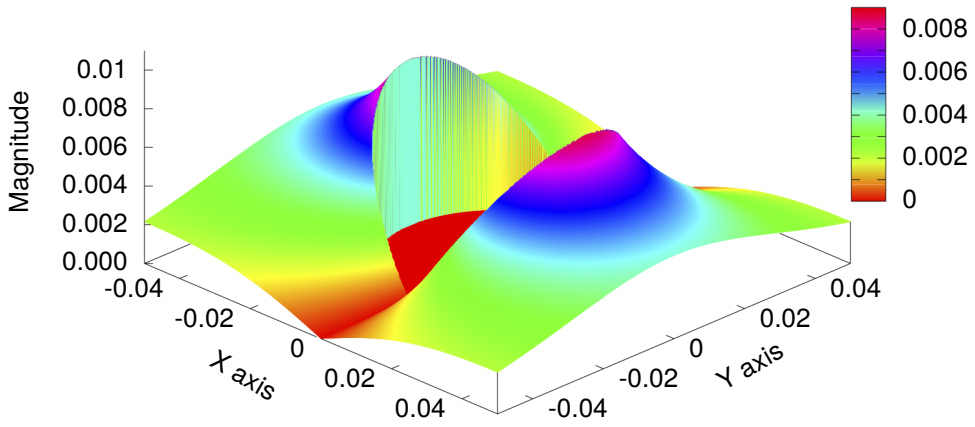

Fig. 23—Exact and approximate H_y fields near a metal cylinder 0.05 meters in diameter at 300 MHz for ϕ^i = 180.

8. APPLICATION OF MODIFIED ASSIGNED MATERIAL PARAMETERS

For the first application of the MAMP concept I consider the 0.05 meter diameter metal cylinder from Figure 19 aligned in the 0.05 meter FDTD grid as shown in Figure 24. From Equation (36) the frequency

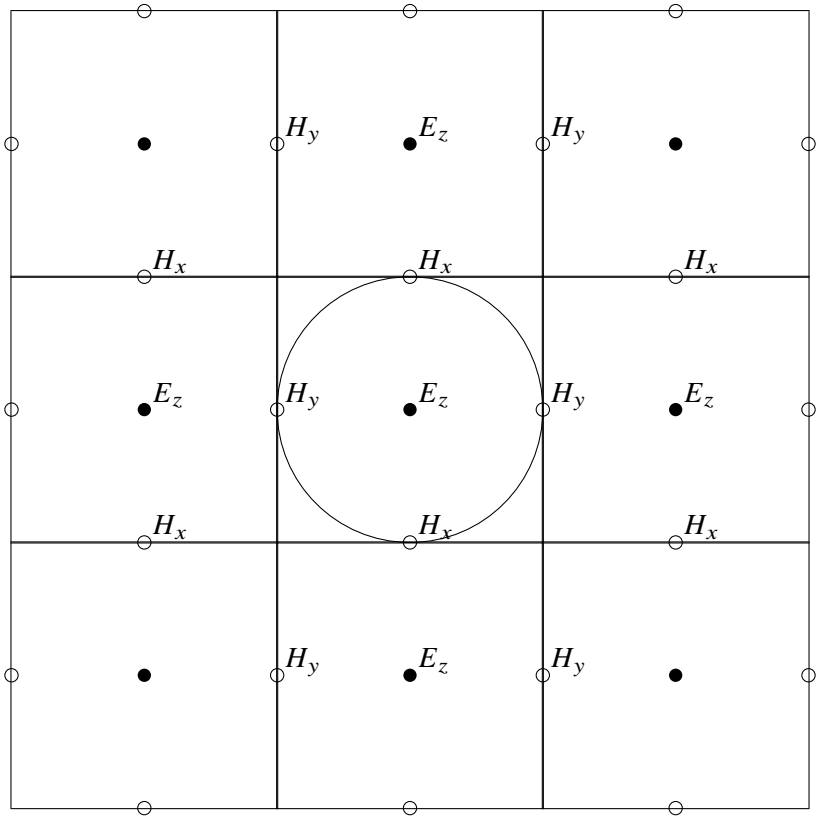

Fig. 24—First example of the MAMP concept applied to a metal cylinder with the same diameter as the FDTD grid size.

dependent $\ln\left(\frac{\gamma}{2}k_0 a\right)$ term in Equation (46) divides out and therefore I have [38, 39]

$$\mathcal{E}_z(x,y) \propto \ln\left[\frac{1}{a}\sqrt{x^2+y^2}\right], \tag{47a}$$

$$\mathcal{H}_x(x,y) \propto \frac{y}{x^2+y^2}, \tag{47b}$$

$$\mathcal{H}_y(x,y) \propto \frac{x}{x^2+y^2}. \tag{47c}$$

From Equations (38b) – (38c) for a cylinder located at the origin, the general μ_x and μ_y correction factors are given by

$$\mu_x(x,y) = \frac{\int_{y-\frac{\Delta y}{2}}^{y+\frac{\Delta y}{2}} \frac{u}{x^2+u^2}du}{\int_{x-\frac{\Delta x}{2}}^{x+\frac{\Delta x}{2}} \frac{y}{u^2+y^2}du}, \tag{48a}$$

$$\mu_y(x,y) = \frac{\int_{x-\frac{\Delta x}{2}}^{x+\frac{\Delta x}{2}} \frac{u}{u^2+y^2}du}{\int_{y-\frac{\Delta y}{2}}^{y+\frac{\Delta y}{2}} \frac{x}{x^2+u^2}du}, \tag{48b}$$

which can be integrated analytically to give

$$\mu_x(x,y) = \frac{1}{2}\frac{\ln\left(\frac{\left[y+\frac{\Delta y}{2}\right]^2+x^2}{\left[y-\frac{\Delta y}{2}\right]^2+x^2}\right)}{\tan^{-1}\left[\frac{x+\frac{\Delta x}{2}}{y}\right]-\tan^{-1}\left[\frac{x-\frac{\Delta x}{2}}{y}\right]}, \tag{49a}$$

$$\mu_y(x,y) = \frac{1}{2}\frac{\ln\left(\frac{\left[x+\frac{\Delta x}{2}\right]^2+y^2}{\left[x-\frac{\Delta x}{2}\right]^2+y^2}\right)}{\tan^{-1}\left[\frac{y+\frac{\Delta y}{2}}{x}\right]-\tan^{-1}\left[\frac{y-\frac{\Delta y}{2}}{x}\right]}. \tag{49b}$$

The four H field points on the surface of the cylinder are the most significant correction factors, which after adjusting the integration limits to account for zero fields inside the cylinder, are given by [38, 39]

$$\mu_x(x=0, y=\tfrac{\Delta y}{2}) = \frac{\ln\left(\frac{\Delta y}{a}\right)}{2\tan^{-1}\left[\frac{\Delta x}{\Delta y}\right]}, \tag{50a}$$

$$\mu_x(x=0, y=-\tfrac{\Delta y}{2}) = \frac{\ln\left(\frac{a}{\Delta y}\right)}{-2\tan^{-1}\left[\frac{\Delta x}{\Delta y}\right]}, \tag{50b}$$

$$\mu_y(x=\tfrac{\Delta x}{2}, y=0) = \frac{\ln\left(\frac{\Delta x}{a}\right)}{2\tan^{-1}\left[\frac{\Delta y}{\Delta x}\right]}, \tag{50c}$$

$$\mu_y(x=-\tfrac{\Delta x}{2}, y=0) = \frac{\ln\left(\frac{a}{\Delta x}\right)}{-2\tan^{-1}\left[\frac{\Delta y}{\Delta x}\right]}. \tag{50d}$$

Modifying the FDTD parameters for just these four points corrects for about one-half the difference between the FDTD scattering from the single E_z field point and the exact eigenfunction solution as seen in Figure 25. Using Equations (49) – (50), I extend the MAMP calculations to all H field points within one cell of the cylinder surface; however, I do not see further improvement in the scattered field, as seen in Figure 26. What

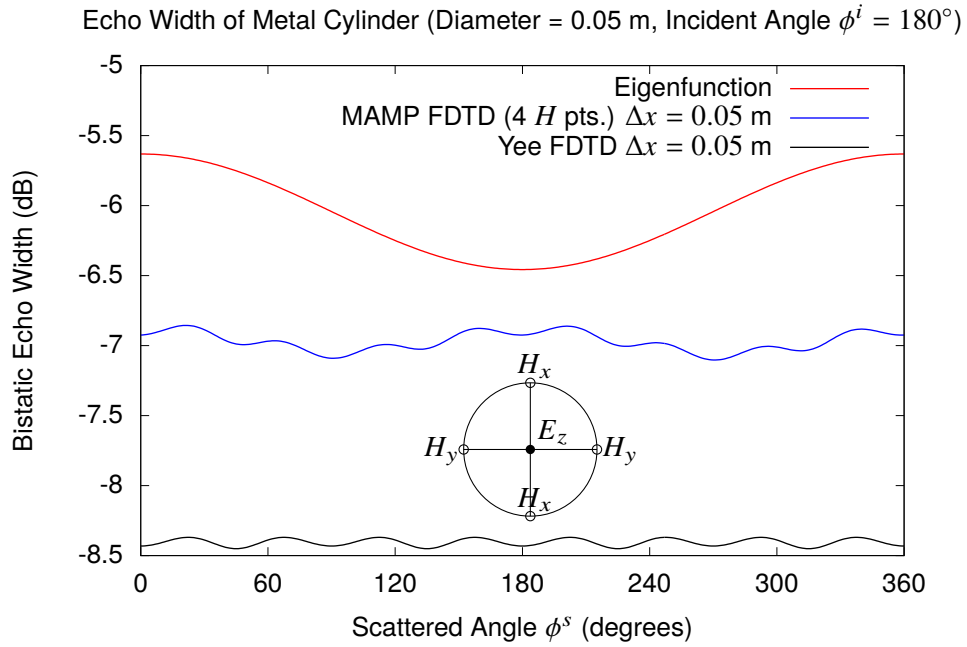

Fig. 25—Bistatic echo width of a metal cylinder 0.05 meters in diameter at 300 MHz for the exact analytic eigenfunction solution versus the MAMP FDTD solution with four modified parameters for $\Delta x = 0.05$ meters.

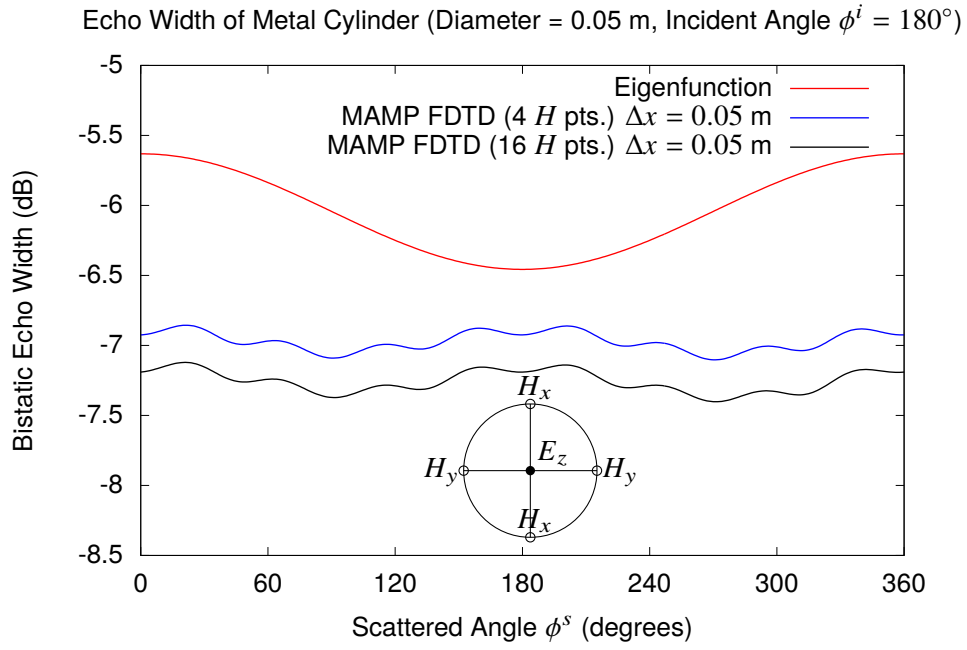

Fig. 26—Bistatic echo width of a metal cylinder 0.05 meters in diameter at 300 MHz for the exact analytic eigenfunction solution versus the MAMP FDTD solution with modified H field parameters for $\Delta x = 0.05$ meters.

is missing at this point is the MAMP's ϵ_z correction factor, which is given by

$$\epsilon_z(x,y) = \frac{1}{\ln\left[\frac{1}{a}\sqrt{x^2+y^2}\right]} \int_{y-\frac{\Delta y}{2}}^{y+\frac{\Delta y}{2}} \int_{x-\frac{\Delta x}{2}}^{x+\frac{\Delta x}{2}} \ln\left[\frac{1}{a}\sqrt{u^2+v^2}\right] du\, dv. \tag{51}$$

Analytical integration of this double integral requires a number of steps, starting with an rearrangement using logarithmic properties, which gives me

$$\epsilon_z(x,y) = \frac{1}{\ln\left[\frac{1}{a}\sqrt{x^2+y^2}\right]} \left\{ \frac{1}{2} \int_{y-\frac{\Delta y}{2}}^{y+\frac{\Delta y}{2}} \int_{x-\frac{\Delta x}{2}}^{x+\frac{\Delta x}{2}} \ln\left(u^2+v^2\right) du\, dv - \int_{y-\frac{\Delta y}{2}}^{y+\frac{\Delta y}{2}} \int_{x-\frac{\Delta x}{2}}^{x+\frac{\Delta x}{2}} \ln(a)\, du\, dv \right\}. \tag{52}$$

Next, using the integration rule from [44, Eq. 2.733.1], I get

$$\epsilon_z(x,y) = \frac{1}{\ln\left[\frac{1}{a}\sqrt{x^2+y^2}\right]} \left\{ \int_{y-\frac{\Delta y}{2}}^{y+\frac{\Delta y}{2}} \left[\frac{u}{2} \ln\left(u^2+v^2\right) - u + v \tan^{-1}\frac{u}{v} \right]_{u=x-\frac{\Delta x}{2}}^{u=x+\frac{\Delta x}{2}} dv - \Delta y\, \Delta x\, \ln(a) \right\}. \tag{53}$$

Using the trigonometric relationship between inverse tangent and inverse cotangent, I get

$$\epsilon_z(x,y) = \frac{1}{\ln\left[\frac{1}{a}\sqrt{x^2+y^2}\right]} \left\{ \left[\int_{y-\frac{\Delta y}{2}}^{y+\frac{\Delta y}{2}} \frac{u}{2} \ln\left(u^2+v^2\right) - u + v \cot^{-1}\frac{v}{u}\, dv \right]_{u=x-\frac{\Delta x}{2}}^{u=x+\frac{\Delta x}{2}} - \Delta y\, \Delta x\, \ln(a) \right\}. \tag{54}$$

Next, using the integration rules from [44, Eq. 2.733.1 and Eq. 2.853.2], I get the asymmetric result

$$\begin{aligned} \epsilon_z(x,y) = \frac{1}{\ln\left[\frac{1}{a}\sqrt{x^2+y^2}\right]} \Bigg\{ \Bigg[\Bigg[& \frac{uv}{2} \ln\left(u^2+v^2\right) - uv + u^2 \tan^{-1}\frac{v}{u} - uv \\ & + \frac{1}{2}(v^2+u^2) \cot^{-1}\frac{v}{u} + \frac{uv}{2} \Bigg]_{v=y-\frac{\Delta y}{2}}^{v=y+\frac{\Delta y}{2}} \Bigg]_{u=x-\frac{\Delta x}{2}}^{u=x+\frac{\Delta x}{2}} - \Delta y\, \Delta x\, \ln(a) \Bigg\}. \end{aligned} \tag{55}$$

As I know the result should be symmetric in u and v, I use another trigonometric property for inverse tangent and cotangent to get the almost symmetric result

$$\begin{aligned} \epsilon_z(x,y) = \frac{1}{\ln\left[\frac{1}{a}\sqrt{x^2+y^2}\right]} \Bigg\{ \Bigg[\Bigg[& \frac{uv}{2} \ln\left(u^2+v^2\right) - \frac{3uv}{2} + \frac{u^2}{2} \tan^{-1}\frac{v}{u} + \frac{v^2}{2} \tan^{-1}\frac{u}{v} \\ & + \frac{\pi u^2}{4} \Bigg]_{v=y-\frac{\Delta y}{2}}^{v=y+\frac{\Delta y}{2}} \Bigg]_{u=x-\frac{\Delta x}{2}}^{u=x+\frac{\Delta x}{2}} - \Delta y\, \Delta x\, \ln(a) \Bigg\}. \end{aligned} \tag{56}$$

Next, evaluating the v integration and simplifying, I get

$$\epsilon_z(x,y) = \frac{1}{\ln\left[\frac{1}{a}\sqrt{x^2+y^2}\right]}\left\{\left[\frac{uy_2}{2}\ln\left(u^2+y_2^2\right) - \frac{uy_1}{2}\ln\left(u^2+y_1^2\right) - \frac{3u\Delta y}{2}\right.\right.$$
$$+\frac{u^2}{2}\left(\tan^{-1}\frac{y_2}{u} - \tan^{-1}\frac{y_1}{u}\right) \tag{57}$$
$$\left.\left.+\frac{y_2^2}{2}\tan^{-1}\frac{u}{y_2} - \frac{y_1^2}{2}\tan^{-1}\frac{u}{y_1}\right]_{u=x-\frac{\Delta x}{2}}^{u=x+\frac{\Delta x}{2}} - \Delta y\,\Delta x\,\ln(a)\right\},$$

where $y_1 = y - \frac{\Delta y}{2}$, $y_2 = y + \frac{\Delta y}{2}$, and the asymmetric term evaluated to zero. Next, evaluating the u integration and simplifying, I get the symmetric result

$$\epsilon_z(x,y) = \frac{1}{\ln\left[\frac{1}{a}\sqrt{x^2+y^2}\right]}\left\{\left[\frac{x_2y_2}{2}\ln\left(x_2^2+y_2^2\right) - \frac{x_1y_2}{2}\ln\left(x_1^2+y_2^2\right)\right.\right.$$
$$-\frac{x_2y_1}{2}\ln\left(x_2^2+y_1^2\right) + \frac{x_1y_1}{2}\ln\left(x_1^2+y_1^2\right) - \Delta x\Delta y\left(\frac{3}{2}+\ln(a)\right)$$
$$+\frac{x_2^2}{2}\left(\tan^{-1}\frac{y_2}{x_2} - \tan^{-1}\frac{y_1}{x_2}\right) - \frac{x_1^2}{2}\left(\tan^{-1}\frac{y_2}{x_1} - \tan^{-1}\frac{y_1}{x_1}\right) \tag{58}$$
$$\left.+\frac{y_2^2}{2}\left(\tan^{-1}\frac{x_2}{y_2} - \tan^{-1}\frac{x_1}{y_2}\right) - \frac{y_1^2}{2}\left(\tan^{-1}\frac{x_2}{y_1} - \tan^{-1}\frac{x_1}{y_1}\right)\right\},$$

where $x_1 = x - \frac{\Delta x}{2}$ and $x_2 = x + \frac{\Delta x}{2}$. Unfortunately, the inclusion of the ϵ_z parameters does not improve the results, as seen in Figure 27. In this specific case, the results including the eight ϵ_z corrections are graphically identical to the results which included only the sixteen $\mu_{x,y}$ corrections. All the analytically calculated MAMP coefficients used in this calculation are shown in Figure 28. Numerical integration is an alternative to analytical calculation of the MAMP coefficients and critical for the generalization of the MAMP concept. For the numerical integration I use Bode's rule (the five-point Newton Cotes rule) [43, Eq. 25.4.14], with the analytical fields from Equation (47). The resulting MAMP coefficients are shown in Figure 29. From a comparison of Figures 28 and 29, I conclude that the analytical and numerical integration are both correctly implemented judged by the close correlation between the analytical and numerical results. For the μ_x and μ_y coefficients on the surface of the cylinder I need to adjust the numerical integration limits as including the zero field points in the integration not only reduces the number of integration points but also creates a discontinuous function that is hard to numerically integrate accurately.

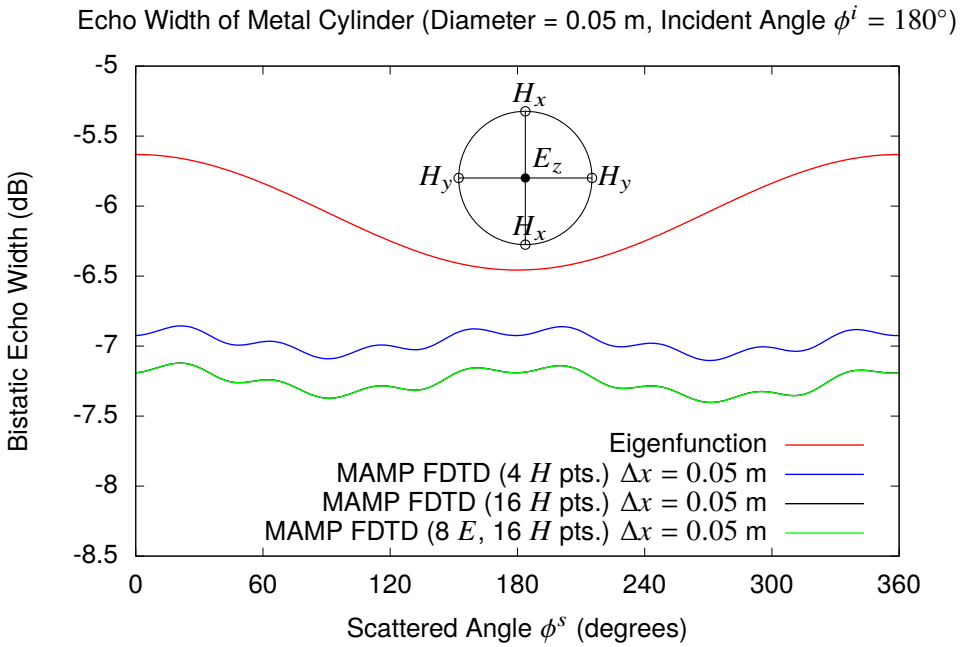

Fig. 27—Bistatic echo width of a metal cylinder 0.05 meters in diameter at 300 MHz for the exact analytic eigenfunction solution versus the MAMP FDTD solution with modified E and H field parameters for $\Delta x = 0.05$ meters.

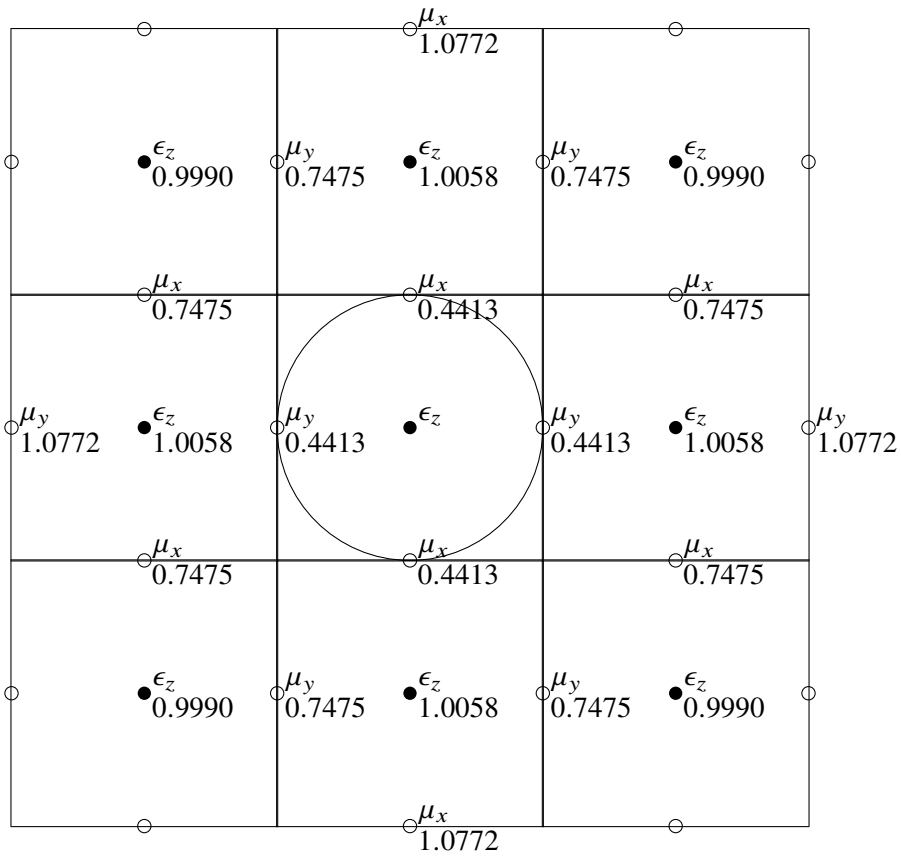

Fig. 28—Analytically calculated MAMP coefficients for metal cylinder with the same diameter as the FDTD grid size.

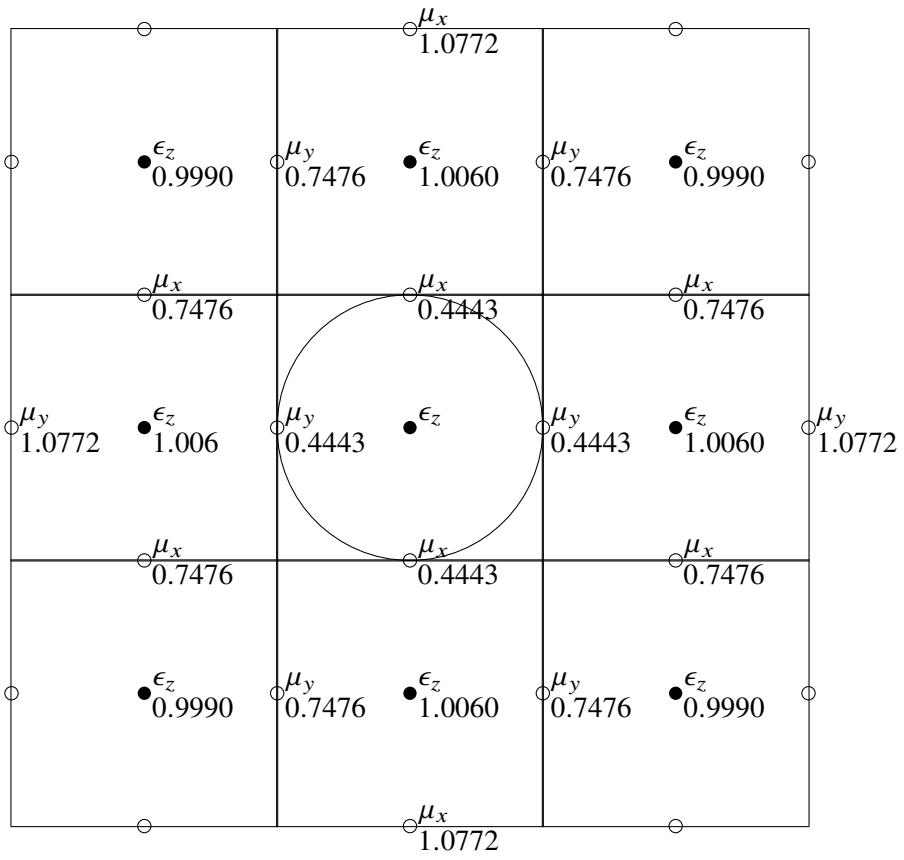

Fig. 29—Numerically calculated MAMP coefficients using Bode's integration rule for metal cylinder with the same diameter as the FDTD grid size.

8.1 Enhancing Far-Field Calculations

When I examine the far field calculations in Figures 25 – 27 I see an unusual ripple caused by the far-field integration I chose in Section 3. I aligned the far-field integration surface with the (H_x, H_y) magnetic fields and linearly interpolated the E_z electric fields. Because of the location of these field points the only integration procedure is Riemann sum without further interpolation. In this section I align the far-field integration surface with the electric fields and use cubic interpolation on the magnetic fields. Because of the location of the E_z points, the minimal integration rule I can use is the trapezoidal rule. From Figure 30 I can see that nearly all the ripple in the scattered field is removed by this change. I can see an additional slight reduction in the remaining ripple in Figure 31 where I have switched the far-field integration to Simpson's Rule. However, from Figure 32 I can see that further enhancement to the far-field integration by switching to Bode's Rule is not enough to justify the added complexity.

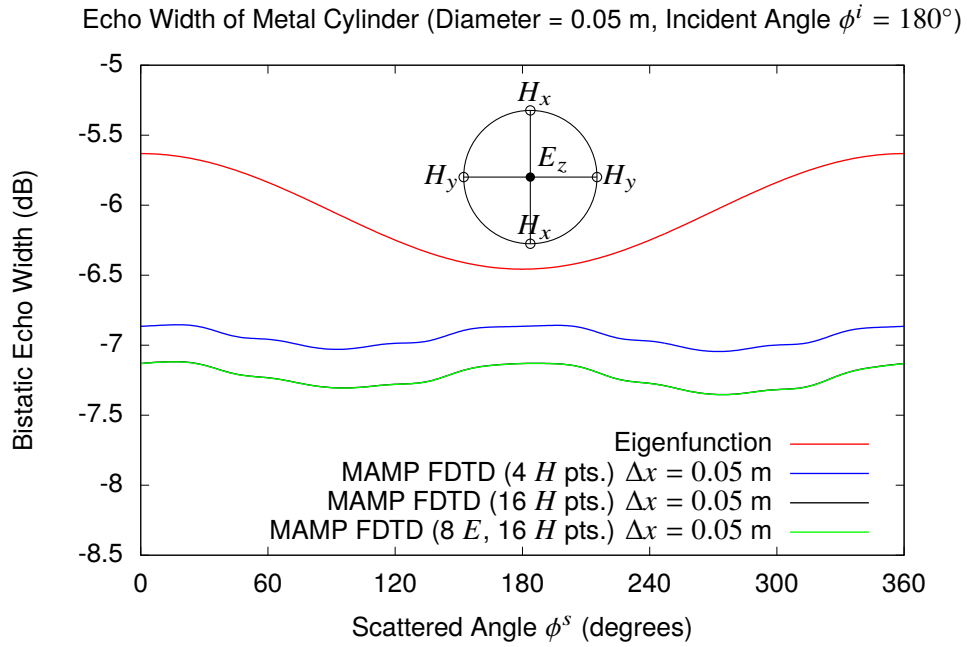

Fig. 30—Trapezoidal rule far-field integration for bistatic echo width of a metal cylinder 0.05 meters in diameter at 300 MHz for the exact analytic eigenfunction solution versus the MAMP FDTD solution with modified E and H field parameters for $\Delta x = 0.05$ meters.

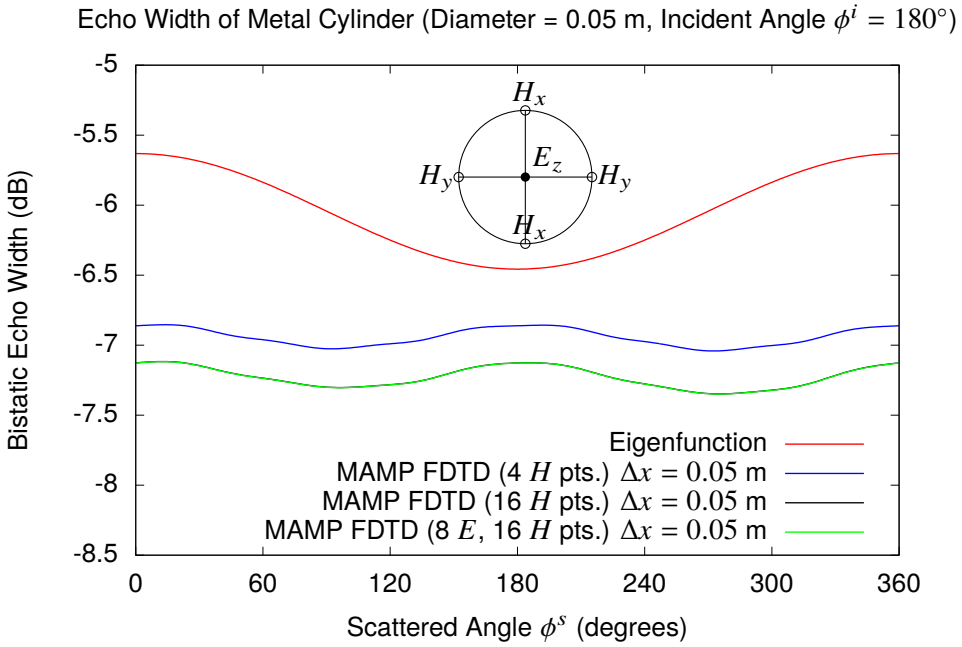

Fig. 31—Simpson's rule far-field integration for bistatic echo width of a metal cylinder 0.05 meters in diameter at 300 MHz for the exact analytic eigenfunction solution versus the MAMP FDTD solution with modified E and H field parameters for $\Delta x = 0.05$ meters.

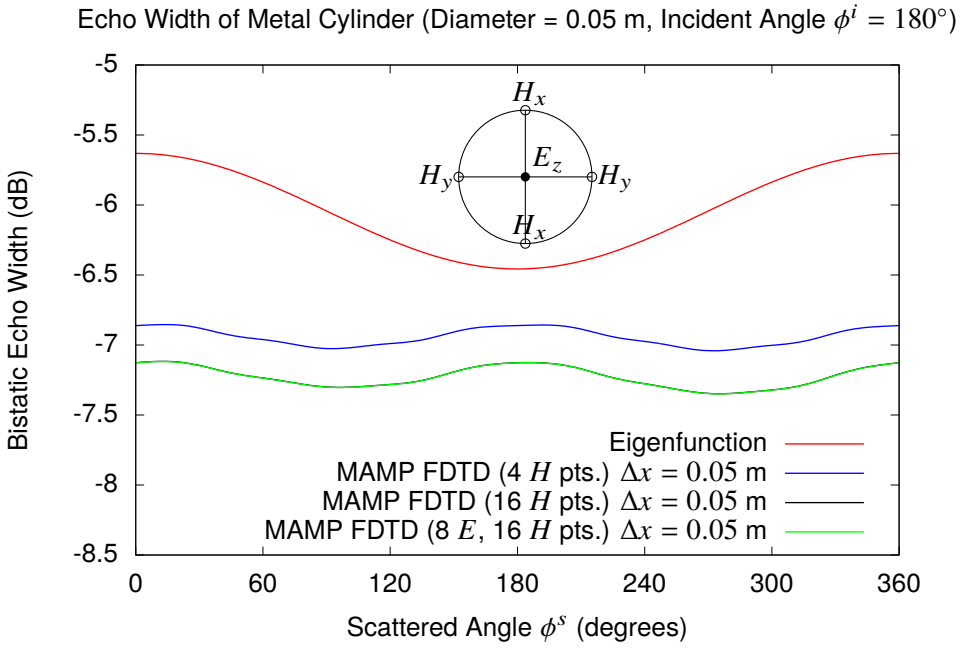

Fig. 32—Bode's rule far-field integration for bistatic echo width of a metal cylinder 0.05 meters in diameter at 300 MHz for the exact analytic eigenfunction solution versus the MAMP FDTD solution with modified E and H field parameters for $\Delta x = 0.05$ meters.

8.2 Further Consideration of Modified Assigned Material Parameters with Quasistatic Cylinder Solution

In this section, I present results for MAMP FDTD scattering from small cylinders for different sizes and locations of the cylinder. Starting with the 0.5 meter diameter cylinder, I move the cylinder one-half a FDTD cell along the x-axis. This puts two E_z points on the surface of the cylinder and the Yee FDTD solution is within 0.5 dB of the eigenfunction solution. The MAMP FDTD solution using numerical integration of the quasistatic cylinder solution is even closer to the eigenfunction solution as seen in Figure 33. For the second

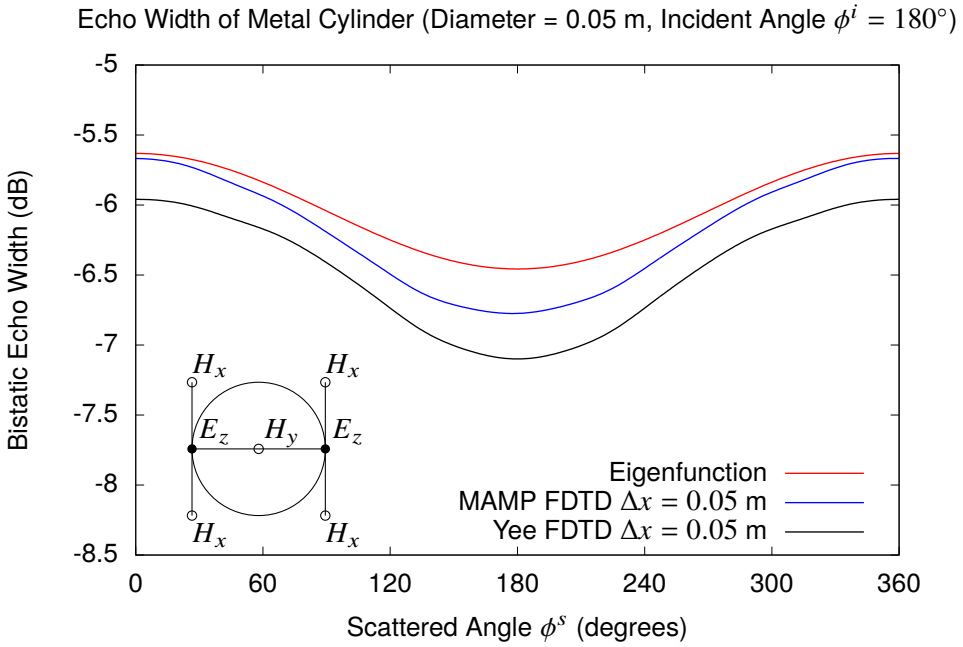

Fig. 33—Bistatic echo width of a metal cylinder 0.05 meters in diameter at 300 MHz for the exact analytic eigenfunction solution versus the MAMP FDTD solution for $\Delta x = 0.05$ meters. The cylinder is centered on a H_y FDTD point resulting in scattering in the FDTD from the two E_z points on the surface of the cylinder.

test case I move the cylinder one-half a FDTD cell along the y-axis. The errors are about 0.7 dB as seen in Figure 34, with the MAMP solution being slightly better than the FDTD solution. In the third case, not shown, I moved the cylinder one-half a FDTD cell along both the x and the y-axes. There is no scattering from the cylinder in the FDTD solution because since no E_z FDTD points are inside the cylinder nor on the surface of the cylinder. The MAMP FDTD results have an average scattering value of -35 dB, which shows a limitation in the MAMP concept. For the next test case I choose a cylinder with a diameter of 0.025 meters centered on a E_z point. The FDTD solution, shown in Figure 35, is the scattering from just the single E_z point, the same as for the cylinder with a diameter of 0.05 meters, first shown in Figure 19. I can see in Figure 35 that the MAMP solution is very accurate for cylinders less than one cell in diameter when the cylinder is centered on a E_z FDTD grid point. For the MAMP solution in Figure 35 I used the analytical MAMP equations, Equations (49) and (58), rather than numerical integration of the quasistatic fields of a small cylinder. Next in Figure 36, I look at the cylinder with a diameter of 0.0708 for the cylinder aligned with four E_z points. With the enhanced far-field integration the FDTD solution does not have the ripple seen in Figure 18. When the integration of the denominator of the MAMP coefficients crosses into the zero

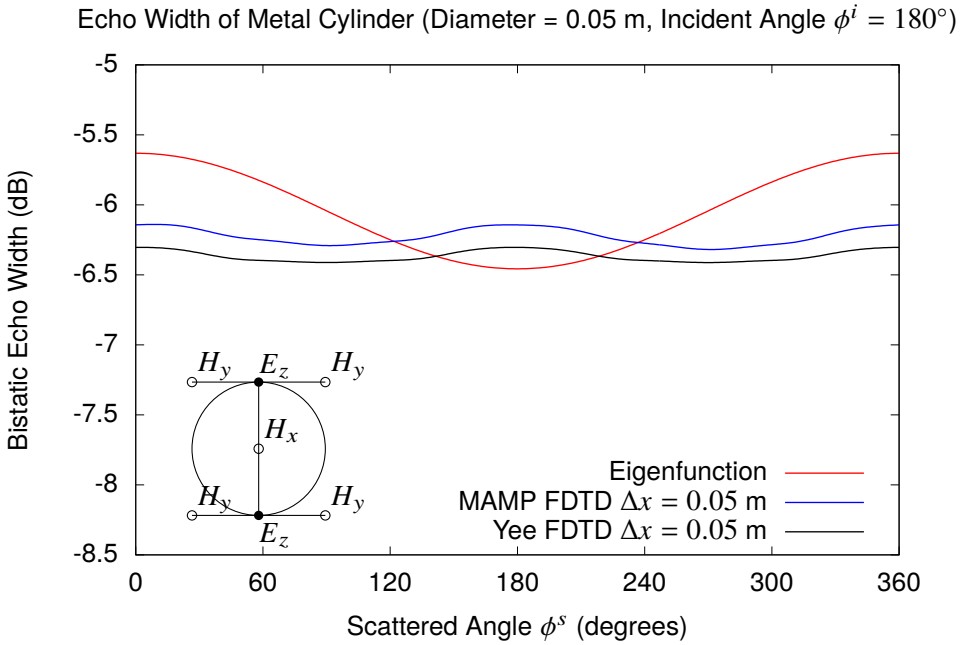

Fig. 34—Bistatic echo width of a metal cylinder 0.05 meters in diameter at 300 MHz for the exact analytic eigenfunction solution versus the MAMP FDTD solution for $\Delta x = 0.05$ meters. The cylinder is centered on a H_x FDTD point resulting in scattering in the FDTD solution from the two E_z points on the surface of the cylinder.

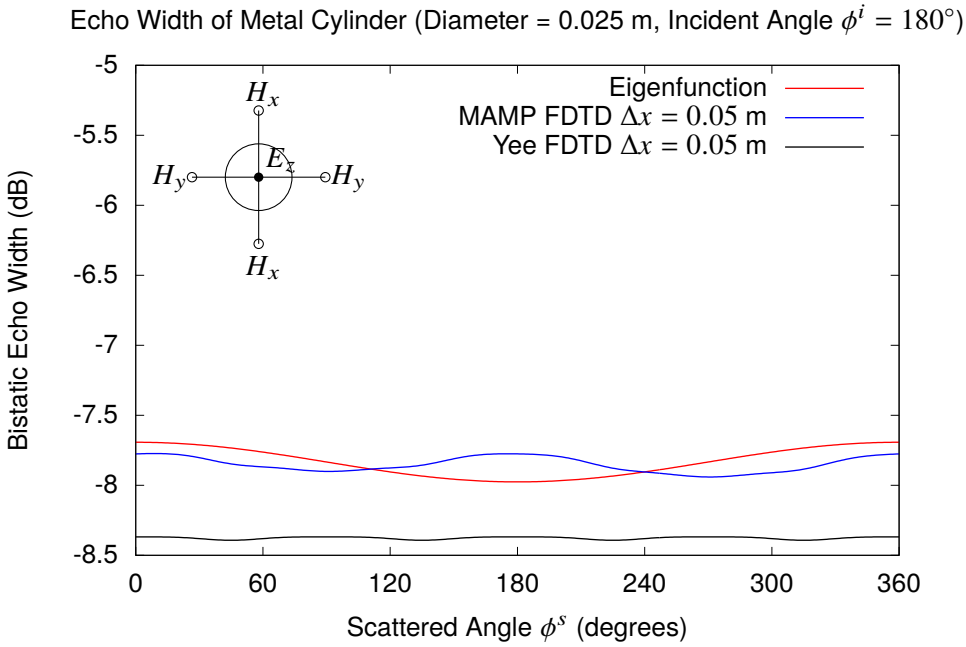

Fig. 35—Bistatic echo width of a metal cylinder 0.025 meters in diameter at 300 MHz for the exact analytic eigenfunction solution versus the MAMP FDTD solution for $\Delta x = 0.05$ meters. The cylinder is centered on a E_z FDTD point resulting in scattering in the FDTD solution from only that point.

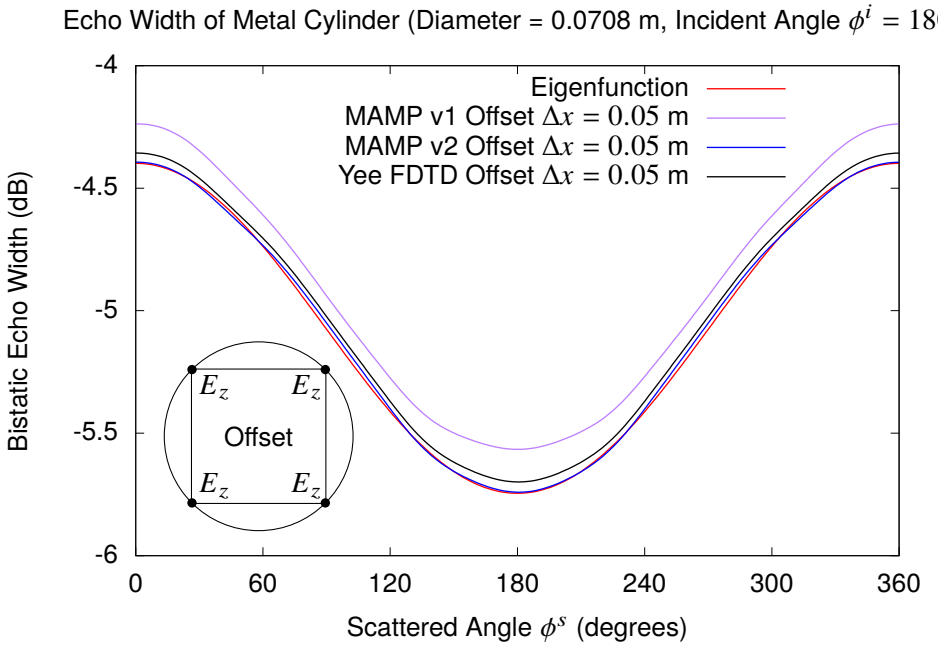

Fig. 36—Bistatic echo width of a metal cylinder 0.0708 meters in diameter at 300 MHz for the exact analytic eigenfunction solution versus the MAMP FDTD solution for $\Delta x = 0.05$ meters.

field region there are two choices, either adjust the integration limits for the zero field region or continue the integration using the quasistatic fields as was done in [38]. In Figure 36, the version 1 MAMP solution is the case where the integration limits in the denominator are adjusted to account for the zero field region. This MAMP solution is not more accurate than the FDTD solution. In contrast, the version 2 MAMP solution in Figure 36 is the case where the integration limits in the denominator are not adjusted and the integration used the continuation of the quasistatic solution for a small cylinder. I see that the version 2 MAMP solution is nearly on top of the eigenfunction solution, even closer than the FDTD solution. However, when this cylinder is centered on a E_z field point in Figure 37, the only scattering in the FDTD solution is from that single E_z field point. Again, I find that the MAMP results are far better when the integration limits in the denominator are not adjusted for the zero field region as seen in Figure 37 (MAMP v2). The difficulty with this solution is that some of the μ_x, μ_y MAMP coefficients are small enough to require a significant reduction in the FDTD time step, Δt. To minimize the side effects of small μ_x, μ_y MAMP coefficients, I next restricted them to be no smaller than 0.3. As seen in Figure 37, this version 3 MAMP is slightly less accurate than version 2; however, the time step adjustment is limited to no greater the 1.8 which still a significant time penalty. Further testing showed no improvement for the cylinder with a diameter of 1.0 meters.

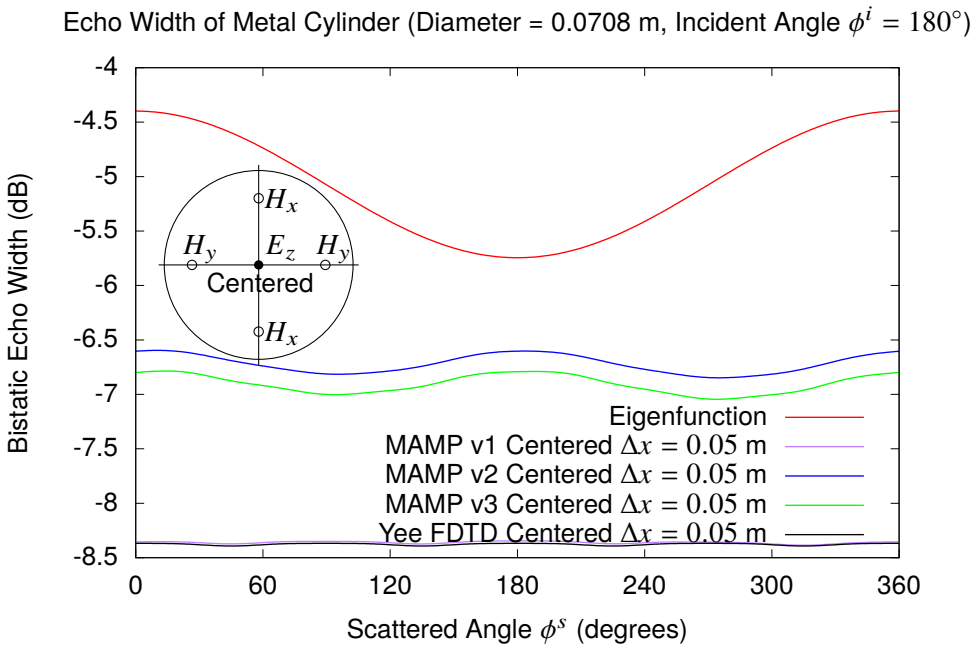

Fig. 37—Bistatic echo width of a metal cylinder 0.0708 meters in diameter at 300 MHz for the exact analytic eigenfunction solution versus the MAMP FDTD solution for $\Delta x = 0.05$ meters.

9. CONCLUSION

This report presented the derivation and evaluation of the Modified Assigned Material Parameters (MAMP) concept as an extension of the finite-difference time-domain (FDTD) method for electromagnetic modeling. In the MAMP concept, a correction factor to the material parameters of a cell is calculated for structures in a cell, thereby accounting for nonlinear field distributions in the cell. As this is equivalent to a physical material, the resulting FDTD equations have the same stability constraints as Yee FDTD. To determine the MAMP coefficients around a cylinder, I used the characteristic near field of a metal cylinder which is derived in this report. To accurately evaluate the MAMP concept, I developed and evaluated enhancements to the total-field/scattered-field method for the generation of an incident plane-wave in two-dimensions. In addition, I showed the errors from a conventional method for the evaluation of the scattered far-field versus alternatives. In summary, I show that MAMP concept provides some increase in accuracy for the scattering by small cylinders, but to be useful in general requires the quasistatic solution for general shapes and further improvement will require a different formulation of the MAMP concept as the required reduction in the time step would require double the computation time.

REFERENCES

1. M. Kluskens, "Developments in the Finite-Difference Time-Domain Method for Electromagnetic Modeling," NRL/MR/5310-20-10,148, U. S. Naval Research Laboratory, Washington, DC, Oct. 2020.

2. R. F. Harrington, *Time-Harmonic Electromagnetic Fields* (McGraw-Hill, New York, 1961).

3. C. A. Balanis, *Advanced Engineering Electromagnetics* (Wiley, New York, 1989).

4. K. S. Kunz and R. J. Luebbers, *The Finite Difference Time Domain Method for Electromagnetics* (CRC Press, Boca Raton, FL, 1993).

5. K. S. Yee, "Numerical Solution of Initial Boundary Value Problems Involving Maxwell's Equations in Isotropic Media," *IEEE Transactions on Antennas and Propagation* **14**(3), 302–307 (Mar. 1966).

6. A. Taflove and S. Hagness, *Computational Electrodynamics: The Finite-Difference Time-Domain Method, 2 ed.* (Artech House, Boston, MA, 2000).

7. J. B. Schneider, "Plane Waves in FDTD Simulations and a Nearly Perfect Total-Field/Scattered-Field Boundary," *IEEE Transactions on Antennas and Propagation* **52**(12), 3280–3287 (Dec. 2004).

8. J. B. Schneider, "Correction to "Plane Wave in FDTD Simulations and a Nearly Perfect Total-Field/Scattered-Field Boundary"," *IEEE Transactions on Antennas and Propagation* **53**(11), 3857 (Nov. 2005).

9. J. B. Schneider and K. Abdijalilov, "Analytic Field Propagation TFSF Boundary for FDTD Problems Involving Planar Interfaces: PECs, TE, and TM," *IEEE Transactions on Antennas and Propagation* **54**(9), 2531–2542 (Sept. 2006).

10. T. Tan and M. Potter, "1-D Multipoint Auxiliary Source Propagator for the Total-Field/Scattered-Field FDTD Formulation," *IEEE Antennas and Wireless Propagation Letters* **6**, 144–148 (2007).

11. I. R. Çapoğlu and G. S. Smith, "A Total-Field/Scattered-Field Plane-Wave Source for the FDTD Analysis of Layered Media," *IEEE Transactions on Antennas and Propagation* **56**(1), 158–169 (Jan. 2008).

12. M. F. Hadi, "A Versatile Split-Field 1-D Propagator for Perfect FDTD Plane Wave Injection," *IEEE Transactions on Antennas and Propagation* **57**(9), 2691–2697 (Sept. 2009).

13. T. Tan and M. Potter, "Optimized Analytic Field Propagator (O-AFP) for Plane Wave Injection in FDTD Simulations," *IEEE Transactions on Antennas and Propagation* **58**(3), 824–831 (Mar. 2010).

14. T. Tan and M. Potter, "FDTD Discrete Planewave (FDTD-DPW) Formulation for a Perfectly Matched Source in TFSF Simulations," *IEEE Transactions on Antennas and Propagation* **58**(8), 2641–2648 (Aug. 2010).

15. H. Kim, I. S. Koh, and J. G. Yook, "Enhanced Total-Field/Scatter-Field Technique for Isotropic-Dispersion FDTD Scheme," *IEEE Transactions on Antennas and Propagation* **58**(10), 3407–3411 (Oct. 2010).

16. R. Bollimuntha, M. F. Hadi, M. J. Piket-May, and A. Z. Elsherbeni, "Dispersion Optimized Plane Wave Sources for Scattering Analysis with Integral Based High Order Finite Difference Time Domain Methods," *IET Microwaves, Antennas & Propagation.* **10**, 976–982 (2016).

17. K. Demarest, R. Plumb, and Z. Huang, "FDTD Modeling of Scatterers in Stratified Media," *IEEE Transactions on Antennas and Propagation* **43**(10), 1164–1168 (Oct. 1995).

18. K. Demarest, Z. Huang, and R. Plumb, "An FDTD Near- to Far-Zone Transformation for Scatterers Buried in Stratified Grounds," *IEEE Transactions on Antennas and Propagation* **44**(8), 1150–1157 (Aug. 1996).

19. K. Abdijalilov and J. B. Schneider, "Analytic Field Propagation TFSF Boundary for FDTD Problems Involving Planar Interfaces: Lossy Material and Evanescent Fields," *IEEE Antennas and Wireless Propagation Letters* **5**, 454–458 (2006).

20. D. Isleifson, I. Jeffrey, L. Shafai, J. Lovetri, and D. Barber, "An Efficient Scattered-Field Formulation for Objects in Layered Media Using the FVTD Method," *IEEE Transactions on Antennas and Propagation* **59**(11), 4162–4170 (Nov. 2011).

21. P. Chen and X. Xu, "Introduction of Oblique Incidence Plane Wave to Stratified Lossy Dispersive Media for FDTD Analysis," *IEEE Transactions on Antennas and Propagation* **60**(8), 3693–3705 (Aug. 2012).

22. G. Evans, *Practical Numerical Integration* (Wiley, New York, 1993).

23. J. J. Bowman, T. B. A. Senior, and P. L. E. Uslenghi, *Electromagnetic and Acoustic Scattering by Simple Shapes* (Hemisphere, New York, 1987).

24. D. T. Shimizu, M. Okoniewski, and M. A. Stuchly, "An Efficient Sub-gridding Algorithm for FDTD," Proceedings of the 11th Annual Review of Progress in Applied Computational Electromagnetics, volume 2, Monterey, CA, Mar. 1995, pp. 762–766.

25. B. Denecker, F. Olyslager, L. Knockaert, and D. De Zutter, "Generation of FDTD Subcell Equations by Means of Reduced Order Modeling," *IEEE Transactions on Antennas and Propagation* **51**(8), 1806–1817 (Aug. 2003).

26. N. V. V. =and R. Lee, Y. B. Gan, and L. W. Li, "A Stable FDTD Subgridding Method Based on Finite Element Formulation With Hanging Variables," *IEEE Transactions on Antennas and Propagation* **55**(3), 907–915 (Mar. 2007).

27. R. A. Chilton and R. Lee, "Conservative and Provably Stable FDTD Subgridding," *IEEE Transactions on Antennas and Propagation* **55**(9), 2537–2549 (Sept. 2007).

28. S. Dey and R. Mittra, "A Locally Conformal Finite Difference Time Domain (FDTD) Algorithm for Modeling 3-D Objects with Curved Surfaces," Proceedings of the IEEE Antennas and Propagat. Soc. Int. Symp., volume 4, Montréal, Canada, July 1997, pp. 2172–2175.

29. S. Dey and R. Mittra, "A Locally Conformal Finite-Difference Time-Domain (FDTD) Algorithm for Modeling Three-Dimensional Perfectly Conducting Objects," *IEEE Microwave Guided Wave Letters* **7**(9), 273–275 (Sept. 1997).

30. S. Dey and R. Mittra, "A Locally Conformal Finite Difference Time Domain Technique for Modeling Arbitrary Shaped Objects," Proceedings of the IEEE Antennas and Propagat. Soc. Int. Symposium, volume 1, Atlanta, GA, June 1998, pp. 584–587.

31. S. Dey and R. Mittra, "A Modified Locally Conformal Finite-Difference Time-Domain Algorithm for Modeling Three-Dimensional Perfectly Conducting Objects," *Microwave and Optical Technology Letters* **17**(6), 349–352 (Apr. 1998).

32. S. Dey, R. Mittra, and N. Pegg, "Efficient and Accurate Calculation of Radar Cross Section of Curved Objects by Using the Conformal Finite Difference Time Domain Method," Proceedings of the IEEE Antennas and Propagat. Soc. Int. Symposium, volume 4, Orlando, FL, July 1999, pp. 2652–2655.

33. S. Dey and R. Mittra, "A Conformal Finite-Difference Time-Domain Technique for Modeling Cylindrical Dielectric Resonantors," *IEEE Transactions on Microwave Theory and Techniques* **47**(9), 1737–1739 (Sept. 1999).

34. D. B. Shorthouse and C. J. Railton, "The Incorporation of Static Field Solutions into the Finite Difference Time Domain Algorithm," *IEEE Transactions on Microwave Theory and Techniques* **40**(5), 986–994 (May 1992).

35. S. M. Foroughipour and K. P. Esselle, "The Theory of a Singularity-Enhanced FDTD Method for Diagonal Metal Edges," *IEEE Transactions on Antennas and Propagation* **51**(2), 312–321 (Feb. 2003).

36. F. Lu and B. Chen, "The Theory of a Singularity-Enhanced Method for Sharp Metal Edge Diagonal to the Cell Cube in FDTD Grid," *IEEE Transactions on Antennas and Propagation* **53**(3), 1203–1214 (Mar. 2005).

37. J. Larsson, "Electromagnetics from a quasistatic perspective," *American Journal of Physics* **75**(3), 230–239 (Mar. 2007), doi:10.1119/1.2397095. URL `http://dx.doi.org/10.1119/1.2397095`.

38. C. J. Railton, D. L. Paul, I. J. Craddock, and G. S. Hilton, "The Treatment of Geometrically Small Structures in FDTD by the Modification of Assigned Material Parameters," *IEEE Transactions on Antennas and Propagation* **53**(12), 4129–4136 (Dec. 2005).

39. C. J. Railton, D. L. Paul, and S. Dumanli, "The Treatment of Thin Wire and Coaxial Structures in Lossless and Lossy Media in FDTD by the Modification of Assigned Material Parameters," *IEEE Transactions on Electromagnetic Compatibility* **48**(4), 654–660 (Nov. 2006).

40. C. J. Railton, D. L. Paul, I. J. Craddock, and G. S. Hilton, "The Treatment of Singularities at 90° and 270° Microstrip Corners in FDTD by the Modification of Assigned Material Parameters," *IEEE Transactions on Antennas and Propagation* **55**(7), 2124–2129 (July 2007).

41. C. J. Railton and D. L. Paul, "Treatment of metal laminas with sharp edges at arbitrary angles to the FDTD grid using MAMPs," Proceedings of the 2009 Loughbori=ough Antennas & Propagation Conference, Loughborough, UK, Nov. 2009, pp. 481–484.

42. C. J. Railton and D. L. Paul, "Analysis of Structures Containing Sharp Oblique Meta Edges in FDTD Using MAMPs," *IEEE Transactions on Antennas and Propagation* **58**(9), 2954–2960 (Sept. 2010).

43. M. Abramowitz and I. A. Stegun, eds., *Handbook of Mathematical Functions*, Appl. Math. Ser. 55 (National Bureau of Standards, Washington, D.C., 1964).

44. I. S. Gradshteyn and I. M. Ryzhik, *Table of Integrals, Series, and Products*, 7th ed. (Academic Press, 2007).

This page intentionally left blank

Appendix A

LIST OF SYMBOLS

ϵ	permittivity (F/m)
ϵ_0	permittivity of free space (8.854×10^{-12} F/m)
η_0	wave impedance of free space, $\sqrt{\mu_0/\epsilon_0}$ (V/A)
γ	≈ 1.781, natural log of Euler's constant, when used in the Bessel series for the term $\ln(\frac{\gamma}{2}x)$
γ	≈ 0.5772, Euler's constant, when used in the Bessel series for the term $\{\ln(\frac{x}{2}) + \gamma\}$
λ_0	wavelength in free space, $c/$ frequency (m)
μ	permeability (H/m)
μ_0	permeability of free space ($4\pi \times 10^{-7}$ H/m)
$\rho(t)$	electric charge density (time-domain, scalar) (C/m^3)
ρ	distance in cylindrical coordinate system (m)
σ	effective electric conductivity (S/m)
σ^*	effective magnetic conductivity (Ω / m)
σ_{2D}	echo width (m)
ϕ^i	incidence angle
ϕ^s	scattered field angle
Δt	FDTD time step (s)
Δx	FDTD spatial step in x direction (m)
Δy	FDTD spatial step in y direction (m)
Ω	ohm, unit of resistance (1 Ω = 1 V/A)
c	speed of light in free space (299,792,458 m/s)
c_a, c_b	parameters in FDTD electric field update equation
d_a, d_b	parameters in FDTD magnetic field update equation
$f(\phi^i)$	dispersion correction factor dependent of incidence angle ϕ^i
f_c	center frequency of a Gaussian pulse (Hz)
f_{BW}	bandwidth of a Gaussian pulse (Hz)
k_0	wavenumber in free space, $2\pi/\lambda$ (1/m)
$\hat{n}$	outward normal to a surface (vector)
s_o	offset to account for PML region in the plane wave excitation of total-field region
x_m	$-x$ boundary of total-field region
x_o	x offset for plane wave excitation of total-field region
x_p	$+x$ boundary of total-field region
y_m	$-y$ boundary of total-field region
y_o	y offset for plane wave excitation of total-field region
y_p	$+y$ boundary of total-field region

A	ampere, unit of current (1 A = 1 C / s)
C	coulomb, unit of charge (1 C = 1 A s)
$\mathbf{E}$	electric field intensity (frequency-domain, vector) (V/m)
$\mathbf{E^R}$	electric field intensity in reciprocal problem (frequency-domain, vector) (V/m)
F	farad, unit of capacitance (1 F = 1 C/V)
H	henry, unit of inductance (1 H = 1 Wb/A)
$\mathbf{H}$	magnetic field intensity (frequency-domain, vector) (A/m)
$\mathbf{H^R}$	magnetic field intensity in reciprocal problem (frequency-domain, vector) (A/m)
$H_n^{(2)}$	Hankel function of the second kind of order n
$J_n(x)$	Bessel function of the first kind of order n
$\mathbf{J}$	electric current density (frequency-domain, vector) (A/m^2)
$\mathbf{J^R}$	electric current density in reciprocal problem (frequency-domain, vector) (A/m^2)
$\mathbf{M}$	magnetic current density (frequency-domain, vector) (V/m^2)
S	siemens, unit of electrical conductivity (1 S = 1 A/V)
V	volt, unit of potential difference (1 V = 1 J / C)
Wb	weber, unit of magnetic flux (1 Wb = 1 V s)
$Y_n(x)$	Bessel function of the second kind of order n
$\mathcal{B}(t)$	magnetic flux density (time-domain, vector) (Wb/m^2)
$\mathcal{D}(t)$	electric flux density (time-domain, vector) (C/m^2)
$\mathcal{E}(t)$	electric field intensity (time-domain, vector) (V/m)
$\mathcal{E}(t)$	electric field intensity (time-domain, scalar) (V/m)
$\mathcal{E}^i(t)$	incident electric field intensity (time-domain, scalar) (V/m)
$\mathcal{E}^t(t)$	electric field intensity in total-field region (time-domain, scalar) (V/m)
$\mathcal{E}^{t'}(t)$	electric field intensity in total-field region uncorrected for incident magnetic field in FDTD update equations (time-domain, scalar) (V/m)
$\mathcal{E}^{1D}(t)$	electric field intensity in one-dimensional FDTD grid (time-domain, scalar) (V/m)
$\mathcal{H}(t)$	magnetic field intensity (time-domain, vector) (A/m)
$\mathcal{H}(t)$	magnetic field intensity (time-domain, scalar) (A/m)
$\mathcal{H}^i(t)$	incident magnetic field intensity (time-domain, scalar) (A/m)
$\mathcal{H}^s(t)$	magnetic field intensity in scattered-field region (time-domain, scalar) (A/m)
$\mathcal{H}^{s'}(t)$	magnetic field intensity in scattered-field region uncorrected for incident electric field in FDTD update equations (time-domain, scalar) (A/m)
$\mathcal{H}^{1D}(t)$	magnetic field intensity in one-dimensional FDTD grid (time-domain, scalar) (A/m)
$\mathcal{J}(t)$	electric current density (time-domain, vector) (A/m^2)
$\mathcal{R}$	a region surrounded by a surface $\mathcal{S}$
$\mathcal{S}$	a surface surrounding a region $\mathcal{R}$